UNIVERSITY OF CALIFORNIA SAN DIEGO

Development of mechanogenetic tools for subcellular applications in cancer immunotherapy

A dissertation submitted in partial satisfaction of the requirements for the degree of

Doctor of Philosophy

in

Bioengineering

by

Yijia Pan

Committee in charge:

Professor Yingxiao Wang, Chair
Professor Shu Chien, Co-Chair
Professor Michael W. Berns
Professor Andrew M. Lowy
Professor Anjana Rao
Professor Geert W. Schmid-Shoenbein

2018

The Dissertation of Yijia Pan is approved, and it is acceptable in quality and form for publication on microfilm and electronically:

Co-Chair

Chair

University of California San Diego

2018

Dedication

To my Mom and Dad,

I love you.

Table of Contents

Signature Page iii
Dedication iv
Table of Contents v
List of Figures vii
Acknowledgments x
Vita xiv
Abstract of the Dissertation xvi
Chapter 1 Introduction 1
1.1 Synthetic biology into the clinics 1
1.2 Ultrasound into the clinics 2
1.3 Thesis outline 4
1.4 Acknowledgements 5
1.5 References 6
Chapter 2 A Genetically encoded FRET biosensor for visualizing EphA4 activity at different compartments of the plasma membrane 9
2.1 Abstract 9
2.2 Introduction 10
2.3 Materials and Methods 12
2.3.1 DNA construction and plasmid 12
2.3.2 In vitro protein characterization 13
2.3.3 Cell culture and reagents 13
2.3.4 Image acquisition 14
2.4 Results 15
2.4.1 Design of EphA4 biosensor and its characterization in vitro 15
2.4.2 Characterization of the EphA4 biosensor in mammalian cells 16
2.4.3 The EphA4 activity at different compartments of plasma membrane 17
2.4.4 Cytoskeleton regulation is involved in differential EphA4 activation at different compartments of plasma membrane 19
2.5 Discussions 19
2.6 Acknowledgements 21
2.7 References 29
Chapter 3 The development of Laser induced shockwave (LIS) for activation of Piezo1 ion channel 32
3.1 Abstract 32

3.2 Introduction....33
3.3 Materials and Methods....35
3.3.1 DNA plasmid....35
3.3.2 Cell culture and transfection....35
3.3.3 Laser-Shockwave System....35
3.3.4 Laser-induced shockwave (LIS)....36
3.3.5 Image acquisition....37
3.4 Results....38
3.5 Discussions....41
3.6 Acknowledgements....42
3.7 References....52
Chapter 4 The development of remoted controlled mechanogenetics for cancer immunotherapy....55
4.1 Abstract....55
4.2 Introduction....56
4.3 Materials and Methods....57
4.3.1 Ultrasonic Transducer and Stimulation System....57
4.3.2 Image Acquisition....59
4.3.3 Constructs and Plasmids....60
4.3.4 Cell culture and reagents....61
4.3.5 Cell preparation for ultrasound stimulation....61
4.3.6 Gene activation assays....62
4.3.7 Lentiviral Infection of primary T cells....63
4.3.8 Verifying CAR expression on T cells:....63
4.3.9 Quantitation of CD69 surface expression....63
4.3.10 Luciferase based cell killing assay....64
4.4 Results....64
4.5 Discussions....69
4.6 Acknowledgements....70
4.7 References....79
Chapter 5 Conclusion....83
5.1 Conclusion....83
5.2 References....86

List of Figures

Figure 2.1 The design of the FRET-based EphA4 biosensor and in vitro characterization 22

Figure 2.2 The FRET response of EphA4 biosensor in mammalian cells. 23

Figure 2.3 Characterization of EphA4 biosensor candidates. 24

Figure 2.4 FRET response for the EphA4 biosensor in HeLa and HEK293AD-EphA4 cells. 25

Figure 2.5 EphA4 activation in raft-like domains and non-lipid rafts 26

Figure 2.6 FRET responses for the membrane-targeted EphA4 biosensors in MEF and HEK293AD-EphA4 cells 27

Figure 2.7 Actin filaments differentially regulates EphA4 activation at plasma membrane 28

Figure 3.1 Diagram of an integrated system of Laser induced Shockwave (LIS) and FRET imaging 44

Figure 3.2 The Piezo1 dependent calcium influx upon LIS stimulation in HEK cells. 45

Figure 3.3 Characterization of LIS stimulation on HEK293T cells 46

Figure 3.4 The Piezo1-dependent FAK activation upon LIS stimulation in HEK cells 47

Figure 3.5 The Piezo1-dependent calcium and FAK activation upon LIS stimulation in HeLa cells 48

Figure 3.6 The FAK and calcium activation upon Yoda1 stimulation in the Piezo1-expressing HEK cells 49

Figure 3.7 Piezo1 level dependent calcium influx upon Yoda1 stimulation in HEK cells. 50

Figure 3.8 The titration of Yoda1 stimulation in the Piezo1-expressing HEK cells. ...51

Figure 4.1 Design of synthetic genetic circuits remotely activatable by ultrasound 71

Figure 4.2 The ultrasound stimulation system for cells. 72

Figure 4.3 The calibration of ultrasound power to avoid cell damage. 73

Figure 4.4 Characterization of genetic transducing modules (GTMs) remotely activatable by ultrasound 74

Figure 4.5 The calibration of ultrasound effect on ReCoM responses in HEK293T cells. 75

Figure 4.6 Remote-controlled activation of Jurkat T cells with ReCoM.....76

Figure 4.7 The calibration of the ultrasound effect on ReCoM-a (design a) and b (design b) in Jurkat cells. 77

Figure 4.8 Remote-controlled activation of PBMCs with ReCoM.....78

List of Tables

Table 3.1 The radial distribution of shear forces. 37

Acknowledgments

The work presented in this dissertation was a major collaborative effort and would not have been possible without the support of numerous individuals across multiple institutions. First, I would like to acknowledge my advisor, Dr. Yingxiao Wang, for his support and mentorship throughout my graduate studies. I would also like to acknowledge my co-advisor, Dr. Shu Chien, for his advice and support throughout my PhD. It's been a great privilege to work with and learn from these renowned bioengineers who have created a work environment where science, engineering and collaboration flourishes. I would also like to acknowledge our collaborators, without whom this dissertation would not be possible: Dr. Sangpil Yoon, Dr. Kirk Shung, Dr. Linda Shi, Dr. Daryl Preece, Dr. Veronica Gomez. I would also like to thank my committee members Dr. Michael W. Berns, Dr. Andrew M. Lowy, Dr. Anjana Rao, Dr. Geert W. Schmid-Shoenbein for their ideas, advice and support throughout my PhD graduate studies.

I would like to thank all the members, past and present, of the Wang lab for creating a productive yet enjoyable working environment. I would like to acknowledge Drs. Shaoying Lu, Mingxing Ouyang, Jie Sun, Jihye Seong, Taejin Kim, Lei Lei, Li-Jung Lin, Chris Ochs, Xianwei Liu, Jing Zhou, Ziliang Huang, Qin Peng for their inspiring discussions on science and research. I would like to thank lab managers Yi Wang and Dr. Binbin Chen for their help on experiments. I would like to thank my fellow graduate students Molly Allen, Praopim Limsakul, Pengzhi Wang, Yiqian Wu, Rongxue Wan, Ya Gong, Kaiwen Zhang, Eddie Chung, Yiwen Shi, Qin Qin, Lunan

Shao for their assistance and friendship. I would like to thank my mentees Homa, Lisa, Yen, Masaru, Qiming, Ahiram, Shyamprasad, Zhen, Chris Chu and Linshan Zhu for their assistance and inspiration.

I would like to thank the members of my co-advisor Dr. Chien's lab for creating a collaborative environment. I would like to thank Drs. Mark Wang, Sung Sik Hur, Yi-Ting Yeh, Ya-Ju Chang, Julie Li for their collaboration and valuable discussions. I would like to thank Jerry Norwich and Phu Nguyen for their technical assistance.

I appreciate kind administrative supports from Dr. Jan Lenington in the department of bioengineering. I really appreciate the University of California San Diego, Bioengineering graduate program and Institute of Engineering in Medicine (IEM).

Most importantly, I would like to thank my parents for their support, encouragement and unconditional love throughout my life. I would also like to thank all my friends. I'm thankful to the life we are having in San Diego.

Chapter 1, in part, is nearly identical to a submitted review article entitled "Acoustic mechanogenetics" by Pan Y., Zhu L., Yoon S, Wang Y.. The dissertation author was the primary investigator and author of this paper. The authors acknowledge the funding source NIH CA204704, CA209629, GM125379, HL121365, and NSF CBET1360341. NIH K99-GM120493.

Chapter 2, is nearly identical to a submitted article entitled "A genetically encoded FRET biosensor for visualizing EphA4 activity in different compartments of the plasma membrane" by Pan Y., Lu S., Lei L., Lamberto I., Wang Yi., Pasquale E.B., & Wang Y. The dissertation author was the primary investigator and author of this

paper. The authors acknowledge the funding source NIH CA204704, NSF/NIH Math/Bio Initiative DMS-1361421 (S.L. and Y.W.), NIH HL121365, GM125379, CA209629, NSF CBET1360341 (Y. Wang) and NIH NS087070 (E.B.P.).

Chapter 3 is nearly identical to a submitted article entitled "Mechanosensor Piezo1 displays different modes of activation" by Pan Y., Shi L., Gomez-Godinez V., Preece D., Woo S., Lu S., Chien S., Berns MW., & Wang Y.. The authors thank Dr. Ardem Patapoutian for his generosity in providing materials and advice. The dissertation author was the primary investigator and author of this paper. These authors acknowledge the funding source NIH GM125379, CA204704, CA209629, and HL121365 (Y. Wang), NSF CBET1360341, DMS1361421 (Y. Wang and S.L.), the Beckman Laser Institute Foundation, AFOSR FA9550-08-1-0284, Air Force Office of Scientific Research under award number FA9550-17-1-0193, Beckman Laser Institute Inc. Foundation (M.W.B.). This research was also supported by National Natural Science Foundation of China, NSFC 11428207 (Y. Wang).

Chapter 4 is nearly identical to a peer-reviewed article entitled "Mechanogenetics for the remote and noninvasive control of cancer immunotherapy" by Pan Y., Yoon S., Sun J., Huang Z., Lee C., Allen M., Wu Y., Chang YJ., Sadelain M., Shung K.K., Chien S., Wang Y.. This article was published in Proc Natl Acad Sci U S A. 2018 Jan 30;115(5):992-997. The dissertation author was the primary investigator and author of this paper. The authors thank professor Ardem Patapoutian at Scripps Research Institute for the Piezo1 construct. These authors acknowledge the funding source NIH HL121365, GM125379 (S.C. and Y. Wang), CA204704 and

CA209629 (Y. Wang), NSF CBET1360341, DMS1361421 (Y. Wang and S.L.), and the Beckman Laser Institute Foundation.

Vita

2007-2011 Tsinghua University

Bachelor of Science, Biology

2013-2018 University of California, San Diego

Doctor of Philosophy, Bioengineering

Publications

1. **Pan Y.**, Yoon S., Sun J., Huang Z., Lee C., Allen M., Wu Y., Chang YJ, Sadelain M, Shung KK, Chien S, Wang Y. Mechanogenetics for the remote and noninvasive control of cancer immunotherapy. Proc Natl Acad Sci U S A. 2018 Jan 30;115(5):992-997.

2. **Pan Y**, Zhu L., Yoon S, Wang Y. Acoustic mechanogenetics (submitted)

3. **Pan Y.,** Shi L., Gomez-Godinez V., Preece D., Woo S., Lu S., Chien S., Berns MW., & Wang Y. (submitted) Mechanosensor Piezo1 displays different modes of activation

4. **Pan Y.,** Lu S., Lei L., Lamberto I., Wang Yi., Pasquale E.B., & Wang Y. (submitted) A genetically encoded FRET biosensor for visualizing EphA4 activity in different compartments of the plasma membrane

5. Yoon, S*., **Pan Y*.** (*equal contribution), Shung K., & Wang Y. (ready for submission) Single cell level calcium monitoring using dual FRET biosensors under high frequency ultrasound stimulation

6. Huang Z., Wu Y., **Pan Y.**, Allen M., Chang YJ., Chien S., & Wang Y. (In review) A light inducible gene activation system toward controllable cell-based therapeutics

7. Peng Q., Lu S., Shi Y., **Pan Y.**, Limsakul P., Chernov A., Qiu J., Chai X., Wang P., Ji Y., Li J., Strongin A., Verkhusha V., Belmonte J., Ren B., Wang Y., Chien S., & Wang Y. (In review) Single Cell Visualization of Histone Modifications and Chromatin Reorganization During Cell Cycle

8. Gomez-Godinez V., Preece D., Shi L., Khatibzadeh N., Rosales D., **Pan Y.**, Lei L., Wang Y., Berns MW (2015) Laser-induced shockwave paired with FRET: a method to study cell signaling, Microsc Res Tech 78(3): 195.9

9. Lu S., Wang Y., Huang H., **Pan Y.,** Changey E.J., Boppart S.A., Ozer H., Strongin A.Y., Wang Y. (2013) Quantitative FRET imaging to visualize the invasiveness of live breast cancer cells, PLOS ONE, 8(3):e58569

Abstract of the Dissertation

Development of mechanogenetic tools for subcellular applications in cancer immunotherapy

by

Yijia Pan

Doctor of Philosophy in Bioengineering

University of California San Diego, 2018

Professor Yingxiao Wang, Chair

Professor Shu Chien, Co-Chair

Cancer has long ranked as #1 in the view of doctors and health professionals due to its high death rate. Recent development of molecular engineering and synthetic biology sheds lights on cancer diagnosis and treatment. For example, CAR-T based immunotherapy has become an emerging field in cancer therapeutics. However, major challenges still remain for cancer diagnosis and therapeutics, such as time-consuming detection in cancer diagnosis and uncontrolled cytotoxicity in CAR-T therapy.

Therefore, there is a critical need to engineer molecular tools for more rapid and better control of live cells.

Rapid and efficient measurement of cancer cells is a major challenge in early cancer diagnosis. Fluorescent proteins have revolutionized biology by allowing live cell visualization. Therefore, biosensors based on fluorescent proteins could potentially be developed as the point-of-care detection methods of live cancer cells. In chapter 2 we discussed the development of a FRET based EphA4 biosensor. EphA4 is involved in cellular mechanotransduction and is an engaging target for cancer research. We discovered that EphA4 has different activation at subcellular membrane locations in single live cells, which provides powerful tools to monitor the dynamic molecular activities at subcellular compartments.

Various synthetic biology approaches have been adopted for targeted cancer therapeutics. For example, optogenetics integrating optical and genetics has enabled the sensing and control of molecular events in living systems. However, there is a critical need to remotely manipulate live cells with high precision deep in the body. Mechanical manipulation, in contrast to optogenetics, could allow deep and non-invasive control of these cells. Chapter 3 goes on to discuss the combination of developing a laser based mechanical stimulation tools and molecular biosensors to activate and study mechano-sensitive cells. Together, Chapter 2 and Chapter 3 built the basis for developing and integrating engineered molecular tools with novel clinical therapeutic stimulation devices. Chapter 4, as a major work of this thesis, presents the engineering of a remote controlled mechanogenetics system which integrates ultrasound mediated mechanical stimulation and gene activation of anti-CD19CAR for controllable application in cancer

immunotherapy. Collectively, our suite of engineered molecular tools shows potential in extrapolation to advance biomedical and clinical applications.

Chapter 1 Introduction

1.1 Synthetic biology into the clinics

With the developments of science and technology, healthcare has rapidly grown into one of the most emerging fields in human society. Based on the recently released data by the World Health Organization (WHO), cancer is one of the most common diseases, with 14 millions of new cases each year and over 8.8 million deaths. The total expenditure for cancer reaches approximately 125 billion US dollars in 2010 and will be expected to increase to over 150 billion in 2020 (1). In January 2016, "Cancer Moonshot" was announced in the US with a $1 billion initiative to "accelerate our understanding of cancer and its prevention, early detection and cure"(2).

Cancer diagnosis still relies heavily on traditional *in vitro* tissue histopathology, despite the development of new molecular markers. Common treatment methods of cancers mainly reply on radiation, chemical agents or surgical excision. All of these methods destroy plenty of healthy tissue along with tumors, as well as creating off-target effects. Therefore, there is a growing need for the development of new, important cancer diagnostics methods and medical treatments. Point-of-care diagnosis and individualized therapeutics are needed to overcome challenges in cancer detection and treatment.

Synthetic biology based cancer therapy, on the other hand, is an emerging field that shows promise in recent trials. The field of synthetic biology was accelerated by the development of two engineered molecular circuits: a toggle switch (3) and an

oscillator (4) more than 10 years ago. These DNA-encoded synthetic molecular machines were typically engineered into the cells and perform their functions including signaling detection, intercellular communication, gene activation, etc. While synthetic biology is still at its young age, this field is beginning to use its methods and platforms to bring engineering approaches into cancer biology study and therapeutics development (5).

One exciting example is synthetic-biology-based engineering of CAR-T cell therapy. Among these therapies, the anti-CD19 CAR-T cells trials for treatment of B cell cancer can come to a complete remission. However, major challenges remain for CAR-based immunotherapy against solid tumors. For instance, the non-specific targeting of the CAR-T cells against normal/non-malignant tissues (on-target but off-tumor toxicities) can be life-threatening (6). There is hence an urgent need for the control of CAR-T cell activation with a high spatiotemporal precision.

1.2 Ultrasound into the clinics

Ultrasound has been used for more than 50 years as diagnosis and therapeutic tools. Ultrasound imaging using a single element, or an array transducer has long history and is widely used at research laboratories and clinics (7-9). An effort to use ultrasound as therapeutic tools has been surged due to non-invasive, remote, and safe characteristics that can be used to target biological objects ranging from cells to tissue (10-12).

Early 1940s, Karl Theodore Dussik first developed an idea to display cerebral ventricle using transmission ultrasound (13) while ultrasonic surgery was proposed after recognizing benefits of noninvasiveness using thermal ablation (14, 15). Ultrasound

showed a potential as a versatile source for both diagnosis and therapy. In 1950s, Edler and Hertz presented the echocardiography and the development of array transducers advances the ultrasound medical imaging field. Thermal effect by ultrasound was the main mechanism in therapy before the cavitation effect was observed. The cavitation was studied intensively in 1980s and studies proposed cavitation of microbubble as a diagnosis and therapy purposes (16-18). Since then, studies on the effects of ultrasound to biological targets from cells to animals have conducted and shown that ultrasound has capabilities to modulate function and fate of biological targets. Low frequency ultrasound conjugated with microbubble as an amplifier and high frequency ultrasound have demonstrated that noninvasive and specific control of biological targets advances in the field of immunotherapy and drug delivery in vitro. The scale of biological target and the purpose of applications are selectively adjusted by tuning the properties of ultrasound.

The most representative non-thermal interaction between ultrasound waves and biological tissue is the cavitation or acoustically generated cavitation (19). FDA regulates the exposure of ultrasound energy within certain level depending on organs. One of the regulations is Mechanical Index (MI), which explains mechanical impact of ultrasound energy to biological tissue. The relationship between acoustic pressure and the generation of cavitation is presented previously (20, 21). The role of microbubbles as ultrasound contrast agents is to improve echogenicity and image contrast or amplify ultrasound energy for therapeutic purposes. Oscillatory motion of microbubbles under sonication may break blood-brain-barrier (BBB) or lose connective tissues for easier drug delivery (22). By conjugating moieties with microbubble, targeted delivery to a

specific site such as tumors and safe activation by ultrasound sonication remotely can be achieved (23).

Cells constantly encounter physical forces in the forms of shear stress, compression and stretching (24-27). Early applications of acoustic mechanical stimulations were mainly applied at the tissue level with innate mechanosensitivity. Thanks to the development of synthetic biology and cellular/molecular imaging tools, recent studies start to apply ultrasound induced mechanical effect to investigate cellular mechanical signaling pathways. For example, ultrasound was used to actuate functionalized lipid microbubbles covalently attached to single mechanosensitive live cells to study cytoskeleton and RohA/ROCK signaling (28). In a later study, by exogenously expressing an *E.coli*-derived mechanosensitive ion channel MscL in mammalian cells coupled with microbubble, low frequency ultrasound was first demonstrated to induce the engineered mechanochannel opening and calcium influx *in vitro* (29). Subsequently, in worm *Caenorhabditis elegans*, the low-pressure ultrasound was coupled with microbubbles to sensitize specific neurons that endogenously express the mechanosensitive channel TRP-4 and induce neuronal behavior change (11).

1.3 Thesis outline

As discussed, developing molecular tools to visualize and manipulate cellular signaling events can help to address some major limitations in cancer diagnostics and treatment.

Herein I discuss a series of molecular tools engineering development that aims to develop both sensing and therapeutic tools for cancer biology. Chapter 2 discusses the development of a FRET based EphA4 biosensor to study EphA4 activation at membrane microdomains in single live cells. Chapter 3 goes on to discuss the combination of developing a laser based mechanical stimulation tools and molecular biosensors to activate and study engineered cells. Together, Chapter 2 and Chapter 3 built the basis for developing and integrating engineered molecular tools with novel clinical therapeutic devices. Chapters 4, as a major work of this thesis, presents the engineering of a remote controlled mechanogenetics system which integrates ultrasound mediated mechanical stimulation and gene activation of anti-CD19CAR for application in cancer immunotherapy.

1.4 Acknowledgements

Chapter 1, in part, is nearly identical to a submitted review article entitled "Acoustic mechanogenetics" by Pan Y., Zhu L., Yoon S., Wang Y.. The dissertation author was the primary investigator and author of this paper. The authors acknowledge the funding source NIH CA204704, CA209629, GM125379, HL121365, and NSF CBET1360341. NIH K99-GM120493.

1.5 References

1. Montagnana M & Lippi G (2017) Cancer diagnostics: current concepts and future perspectives. *Ann Transl Med* 5(13):268.

2. Singer DS, Jacks T, & Jaffee E (2016) A U.S. "Cancer Moonshot" to accelerate cancer research. *Science* 353(6304):1105-1106.

3. Gardner TS, Cantor CR, & Collins JJ (2000) Construction of a genetic toggle switch in Escherichia coli. *Nature* 403(6767):339-342.

4. Elowitz MB & Leibler S (2000) A synthetic oscillatory network of transcriptional regulators. *Nature* 403(6767):335-338.

5. Ruder WC, Lu T, & Collins JJ (2011) Synthetic Biology Moving into the Clinic. *Science* 333(6047):1248-1252.

6. June CH, O'Connor RS, Kawalekar OU, Ghassemi S, & Milone MC (2018) CAR T cell immunotherapy for human cancer. *Science* 359(6382):1361-1365.

7. Ritter TA, Shrout TR, Tutwiler R, & Shung KK (2002) A 30-MHz piezo-composite ultrasound array for medical imaging applications. *IEEE Trans Ultrason Ferroelectr Freq Control* 49(2):217-230.

8. Cannata JM, Ritter TA, Chen WH, Silverman RH, & Shung KK (2003) Design of efficient, broadband single-element (20-80 MHz) ultrasonic transducers for medical imaging applications. *IEEE Trans Ultrason Ferroelectr Freq Control* 50(11):1548-1557.

9. Shung KK (1987) General engineering principles in diagnostic ultrasound. *IEEE Eng Med Biol Mag* 6(4):7-13.

10. Bourdeau RW, Lee-Gosselin A, Lakshmanan A, Farhadi A, Kumar SR, Nety SP, & Shapiro MG (2018) Acoustic reporter genes for noninvasive imaging of microorganisms in mammalian hosts. *Nature* 553(7686):86-90.

11. Ibsen S, Tong A, Schutt C, Esener S, & Chalasani SH (2015) Sonogenetics is a non-invasive approach to activating neurons in Caenorhabditis elegans. *Nat Commun* 6:8264.

12. Tyler WJ (2012) The mechanobiology of brain function. *Nat Rev Neurosci* 13(12):867-878.

13. Shampo MA & Kyle RA (1995) Karl Theodore Dussik--pioneer in ultrasound. *Mayo Clin Proc* 70(12):1136.

14. Lynn JG, Zwemer RL, Chick AJ, & Miller AE (1942) A NEW METHOD FOR THE GENERATION AND USE OF FOCUSED ULTRASOUND IN EXPERIMENTAL BIOLOGY. *The Journal of General Physiology* 26(2):179.

15. Lynn JG & Putnam TJ (1944) Histology of Cerebral Lesions Produced by Focused Ultrasound. *Am J Pathol* 20(3):637-649.

16. Apfel RE (1981) Acoustic cavitation prediction. *The Journal of the Acoustical Society of America* 69(6):1624-1633.

17. Flynn HG & Church CC (1988) Erratum: transient pulsations of small gas bubbles in water [J. Acoust. Soc. Am. 84, 985-998 (1988)] [corrected and republished]. *J Acoust Soc Am* 84(5):1863-1876.

18. Flynn HG (1982) Generation of transient cavities in liquids by microsecond pulses of ultrasound. *The Journal of the Acoustical Society of America* 72(6):1926-1932.

19. Leighton TG (1994) *The acoustic bubble* (Academic Press, London) pp xxvi, 613 p.

20. Apfel RE & Holland CK (1991) Gauging the likelihood of cavitation from short-pulse, low-duty cycle diagnostic ultrasound. *Ultrasound Med Biol* 17(2):179-185.

21. Holland CK & Apfel RE (1989) An improved theory for the prediction of microcavitation thresholds. *IEEE Trans Ultrason Ferroelectr Freq Control* 36(2):204-208.

22. Downs ME, Buch A, Karakatsani ME, Konofagou EE, & Ferrera VP (2015) Blood-Brain Barrier Opening in Behaving Non-Human Primates via Focused Ultrasound with Systemically Administered Microbubbles. *Sci Rep* 5:15076.

23. Pan Y, Yoon S, Sun J, Huang Z, Lee C, Allen M, Wu Y, Chang YJ, Sadelain M, Shung KK, Chien S, & Wang Y (2018) Mechanogenetics for the remote and noninvasive control of cancer immunotherapy. *Proc Natl Acad Sci U S A* 115(5):992-997.

24. Vogel V & Sheetz M (2006) Local force and geometry sensing regulate cell functions. *Nat Rev Mol Cell Biol* 7(4):265-275.

25. Liang X & Boppart SA (2010) Biomechanical properties of in vivo human skin from dynamic optical coherence elastography. *IEEE Trans Biomed Eng* 57(4):953-959.

26. Egan P, Sinko R, LeDuc PR, & Keten S (2015) The role of mechanics in biological and bio-inspired systems. *Nature communications* 6:7418.

27. Park Y, Best CA, Badizadegan K, Dasari RR, Feld MS, Kuriabova T, Henle ML, Levine AJ, & Popescu G (2010) Measurement of red blood cell mechanics during morphological changes. *Proceedings of the National Academy of Sciences of the United States of America* 107(15):6731-6736.

28. Fan Z, Sun Y, Di C, Tay D, Chen W, Deng CX, & Fu J (2013) Acoustic tweezing cytometry for live-cell subcellular modulation of intracellular cytoskeleton contractility. *Sci Rep* 3:2176.

29. Heureaux J, Chen D, Murray VL, Deng CX, & Liu AP (2014) Activation of a bacterial mechanosensitive channel in mammalian cells by cytoskeletal stress. *Cell Mol Bioeng* 7(3):307-319.

Chapter 2 A Genetically encoded FRET biosensor for visualizing EphA4 activity at different compartments of the plasma membrane

2.1 Abstract

The EhpA4 receptor tyrosine kinase is well known for its pivotal role in development, cancer progression, and neurological disorders. However, how EphA4 kinase activity is regulated in time and space still remains unclear. To visualize EphA4 activity in different membrane microdomains, we developed a sensitive EphA4 biosensor based on Förster resonance energy transfer (FRET), and targeted it in or outside raft-like microdomains in the plasma membrane. We showed that our biosensor can produce a robust and highly specific FRET response upon EphA4 activation, both *in vitro* and in live cells. Interestingly, we observed stronger FRET responses for the non-raft targeting biosensor than for the raft targeting biosensor, suggesting that stronger EphA4 activation may occur in non-raft regions. Further investigations revealed the importance of the actin cytoskeleton in suppressing EphA4 activity in raft-like microdomains. Therefore, our FRET-based EphA4 biosensor could serve as a powerful tool to visualize and investigate EphA4 activation and signaling in specific subcellular compartments of single live cells.

2.2 Introduction

EphA4 belongs to the Eph receptor family, which is the largest family of tyrosine kinase receptors. The Eph receptors are subdivided into two classes, EphAs and EphBs, according to sequence similarities and ligand binding preferences (1). Eph receptors bind to another family of membrane tethered proteins, the ephrin ligands, which include the GPI-linked ephrinAs and the transmembrane ephrinBs. As a general rule, EphAs bind to ephrinA ligands, while EphBs bind preferentially to ephrinBs. EphA4 is an exception, since it binds to both ephrinA and ephrinB ligands (2). Structurally, all Eph receptors share a conserved domain composition. The extracellular region contains the N-terminal ephrin-binding domain, a cysteine-rich portion and two fibronectin type III repeats. The intracellular region includes a membrane-spanning juxtamembrane (JM) segment, a tyrosine kinase domain, a sterile-α motif (SAM) domain and a C-terminal Psd-95, Dlg and ZO1 (PDZ)-binding motif (3).

Eph receptors were initially found to guide growing neuronal processes during development through repulsive effects (4). They have also been implicated in other cell communication processes, including angiogenesis, cell morphogenesis, cell migration, tissue patterning, and neuronal plasticity (2). For example, in the nervous system EphA4 is well known as a classic guidance receptor that promotes axon growth cone collapse (5) and also regulates synaptic plasticity (2). Recent studies have also revealed important roles of EphA4 in many types of human cancers (6, 7), such as breast (8) and lung (9), and glioblastoma (10) by regulating cell migration and invasion (9-11). To mediate such a variety of functions, the activation and signaling of the EphA4 kinase

domain require a highly coordinated regulation in space and time. Upon ligand dependent activation, Eph receptors form higher order clusters (12, 13), which are critical for its signaling function (5). However, how EphA4 activation is regulated in different microdomains of the plasma membrane in live cells remains unclear.

The cell plasma membrane has long been proposed to be more mosaic than fluid (14). It is composed of discrete microdomains with unique physical and biological properties. Raft-like domains are small nano-size compartments enriched with cholesterol, sphingomyelin and saturated fatty acids (15). These microcompartments are involved in intracellular trafficking and signaling (16). Because of their detergent-resistant property, raft-like structures were mainly studied by the detergent extraction method (17). EphA4 was reported to be present in both raft-like and non-raft regions by this method (18). However, the detergent extraction method is disruptive to membrane structure and protein contamination among different fractions during the extraction process is likely to happen (19). Furthermore, how EphA4 activity is dynamically regulated at the membrane compartments also remains unclear. Therefore, the development of more advanced methods is needed to study EphA4 regulation at different subcompartments of the plasma membrane in live cells.

One of the first events in Eph receptor activation is the autophosphorylation of two conserved JM tyrosine residues, including Tyr596 in EphA4. In this study, we have developed a novel EphA4 biosensor to specifically detect phosphorylation of Tyr596 and its subsequent binding to the Src SH2 domain. An improved FRET pair, enhanced CFP (ECFP) and YPet, was utilized to enhance the sensitivity of the biosensor (20). To

monitor EphA4 activity in different microdomains of the plasma membrane, we targeted the EphA4 biosensor either in or outside raft-like regions through lipid modifications, including acylation and prenylation, respectively (21). Using this strategy, this biosensor can be directed to tether in different compartments of the plasma membrane, where local EphA4 activity can be monitored in real time. Our results revealed that EphA4 activation induced by ephrin ligands is differentially regulated in different subdomains of the plasma membrane. Further results indicate that the cytoskeleton plays an important role in regulating differential EphA4 activation at the plasma membrane.

2.3 Materials and Methods

2.3.1 DNA construction and plasmid

The construct of the cytosolic EphA4 biosensor was constructed by polymerase chain reaction (PCR) amplification of the complementary DNA from the c-src SH2 domain with a sense primer containing a SphI site and a reverse primer containing the gene sequence for a flexible linker, a substrate peptide (Y596) derived from EphA4 juxtamembrane (JM) region and a SacI site. Candidates substrates Y596, Y602 were derived from EphA4 juxtamembrane region, Y610 was derived from EphB2 JM region. The PCR products were fused with N-terminal enhanced CFP (ECFP) and a C-terminal YPet. Mutation of Y596F, R175V and C185A were conducted using Quickchange site-directed mutagenesis kit (Stratagene). Constructs were cloned into

pRSETB (Invitrogen) using BamHI/EcoRI for bacterial expression and into pcDNA3' (Invitrogen) using BamHI/EcoRI for mammalian cell expression.

The membrane-targeted Lyn-EphA4 biosensors were constructed by fusing 16 Lyn kinase 18 sequences (MGCIKSKRKDNLNDDE) to the N-termini of EphA4 biosensor by PCR. The KRas-EphA4 biosensor was constructed by fusing 14 KRas-prenylation sequences (KKKKKKSKTKCVIM) to the C-termini of EphA4 biosensor by PCR. The PCR products of Lyn- and KRas- EphA4 were inserted into pcDNA3' for mammalian cell expression.

2.3.2 In vitro protein characterization

EphA4 biosensors were expressed with N-terminal 6 × His tags in Escherichia coli and purified by nickel chelation chromatography. Fluorescence emission ratio of ECFP/YPet (478 nm/526 nm) of the biosensors were measured with an excitation wavelength of 430 nm by a fluorescence plate reader (TECAN, Sapphire II) before and after the addition of 1 mM ATP and EphA4 ($1\mu gml^{-1}$) or src ($1\mu gml^{-1}$, Upstate) or PDGFR ($1\mu gml^{-}1$) kinase in kinase buffer (50 mM Tris·HCl, 100mM NaCl, 10mM $MgCl_2$, 2mM DTT, pH 8).

2.3.3 Cell culture and reagents

HeLa, Mouse embryonic fibroblast (MEF) cells were purchased from ATCC. AD293 EphA4 cell line and AD293 EphA4 null control cell line were obtained from Dr. Elena Pasquale's laboratory. Cell culture reagents were obtained from Invitrogen. Cells were maintained in Dulbecco's modified Eagle medium (DMEM) supplemented with 10% fetal bovine serum (FBS), 2 mM L-glutamine, 1 unit/ml penicillin, 100 μg/ml

streptomycin, and 1 mM sodium pyruvate. Cells were cultured in a humidified 95% air, 5% CO_2 incubator at 37 °C. Lipofectamine 2000 (Invitrogen) was used for transfection of DNA plasmids.

1 mM pervanadate solution was prepared as previously described (22). 10 ml of 100 mM Na_3VO_4 and 50 ml 0.3% H_2O_2 in 20 mM HEPES (pH 7.3) were mixed in 940 ml H_2O. 5 min later, catalase (CalBiochem, 260 U/ml) was added to release excess H_2O_2.

Recombinant human ephrin-A3 Fc chimera (R&D systems, Minneapolis, MN) was pre-clustered using anti-human IgG (Jackson Immuno Research, West Grove, PA) for 1 h at room temperature in a 5:1 molar ratio for original EphA4 biosensors. Recombinant mouse ephrin-A1 Fc chimera (R&D systems, Minneapolis, MN) was directly used as stimulant for EphA4 biosensors due to the similar activation effect tested. Platelet-derived growth factor (PDGF) were purchased from Sigma.

2.3.4 Image acquisition

Cells were starved in 0.5% fetal bovine serum for 36-48 h before imaging. During imaging, the cells were cultured in cover-glass-bottom dishes and maintained in 0.5% FBS DMEM medium with 5% CO_2 supplement at 37 °C. Images were collected by a Nikon and a cooled charge-coupled device (CCD) camera using MetaFluor 6.2 and MetaMorph software (Universal Imaging) with a 420DF20 excitation filter, a 455DCXRU dichroic mirror, and two emission filters controlled by a filter changer (480DF40 for CFP and 535DF25 for YFP). A neutral density filter was used to control the intensity of the excitation light. The fluorescence intensity of non-transfected cells was quantified as the background signals and subtracted from the CFP and YFP signals

on transfected cells. The pixel-by-pixel ratio images of CFP/YFP were calculated based on the background-subtracted fluorescence intensity images of CFP and YFP by the Metafluor program to allow quantification and statistical analysis of FRET responses. The emission ratio images were shown in the intensity modified display (IMD) mode(23).

2.4 Results

2.4.1 Design of EphA4 biosensor and its characterization in vitro

We developed a FRET–based EphA4 biosensor, with a central segment containing the SH2 domain of c-Src, a flexible linker peptide, and a specific substrate sequence, concatenated between ECFP and YPet (Figure 2.1A-B). We tested 3 candidates substrate sequences (24), including two substrates derived from EphA4 juxtamembrane (JM) domain and one substrate from EphB2 JM region (See Materials and Methods). Due to its overall efficiency and specificity among the substrate sequences tested, the EphA4 JM region encompassing Tyr596 was selected as our biosensor substrate (Figure 2.2). In our design, the active EphA4 kinase can phosphorylate Tyr596 in the substrate peptide, which subsequently binds intramolecularly to the SH2 domain, causing a conformational change. This conformational change alters the distance or relative orientation between cyan and yellow fluorescent proteins (ECFP and YPet, respectively) inducing a decrease in FRET signal (Figure 2.1B). The purified EphA4 biosensor protein showed a robust FRET signal: upon incubation with EphA4 kinase, the ECFP emission peak of the biosensor

increased, while the YPet emission peak decreased (Figure 2.1C). This result suggests an increase in the ECFP/YPet emission ratio and hence a decrease in the FRET of the biosensor upon phosphorylation by activated EphA4. This FRET response was eliminated by mutation of Tyr596 to Phe in the substrate peptide, or mutation of Arg175 to Val in the binding site of the SH2 peptide (Figure 2.1D). Importantly, no changes in FRET signal was observed upon incubation with the platelet-derived growth factor (PDGF) receptor. On the other hand, a moderate and slow biosensor response occurred with upon incubation with Src (Figure 2.1D). These results suggest that the EphA4 biosensor reports EphA4 activity with relatively high efficiency and specificity *in vitro*.

2.4.2 Characterization of the EphA4 biosensor in mammalian cells

Next we examined the performance of the EphA4 biosensor in mammalian cells. The ROS generator pervanadate (PVD, 20 μM) inhibits tyrosine phosphatases and hence activates Eph receptors (25). Therefore, PVD was used to stimulate the biosensor in live HeLa cells, which are known to express endogenous EphA4 (26). Upon PVD stimulation, a 100% FRET change was observed (Figure 2.3A-B). This suggests that the EphA4 biosensor is capable of undergoing a FRET change upon phosphorylation in live cells.

Following this initial test, different ephrin ligands were used to activate EphA4 and examine biosensor responsiveness. Upon EphA4 activation by stimulation with ephrinA3 or ephrinA1, two ligands known to activate EphA4, a 20% FRET change was observed (Figure 2.3C-D, Figure 2.4). This suggests that the EphA4 biosensor can detect

ligand-induced EphA4 activation in mammalian cells. The mutation of either Tyr596 to Phe (Y596F) in the substrate, or Arg175 to Val (R175V) in the SH2 domain of the biosensor, eliminated the FRET response of the EphA4 biosensor upon ephrinA3 stimulation (Figure 2.3D). These results corroborate our strategy based on the idea that the FRET response of the biosensor following EphA4 activation is due to the intramolecular interaction between the phosphorylated Tyr596 substrate and the Src SH2 domain.

To further examine the specificity of the EphA4 biosensor, 293AD cells engineered to express the EphA4 receptor were tested together with the parental 293AD cells which do not express EphA4. Upon ligand stimulation, a significant FRET response was observed in the EphA4 expressing cells while no obvious signal was detected in the EphA4 null cells (Figure 2.4). Collectively, these results suggest that the EphA4 biosensor can detect the EphA4 activity with high sensitivity in mammalian cells.

2.4.3 The EphA4 activity at different compartments of plasma membrane

EphA4 is a transmembrane receptor and it's activated at the plasma membrane, which contains different microdomains. To study EphA4 regulation in these subcompartments, we further developed EphA4 biosensors targeting to different microdomains of the plasma membranes by modifying the biosensor with the KRas or Lyn membrane-targeting motifs. The KRas biosensor, which localizes in membrane regions outside raft-like regions, was constructed by fusing a prenylation motif derived from KRAS to the C-terminus of the cytosolic EphA4 (cyto-EphA4) biosensor (Fig.

3A). In parallel, a raft-like microdomain targeting motif containing myristoylation and palmitoylation sites (glycine and cysteine) derived from Lyn kinase, was fused to the N-terminus of the cytosolic EphA4 biosensor to generate the EphA4 biosensor that can specifically be located in raft-like regions (Figure 2.5A).

For this experiment we examined EphA4 activation in membrane microdomains of MEF cells. At first, the KRas- and Lyn-EphA4 biosensors were examined by PVD stimulation in MEF. Similar FRET responses were observed (Figure 2.5B-C), suggesting that different localization did not affect activation capability of EphA4 in different microdomains. However, in response to ephrinA3 stimulation, the KRas-EphA4 biosensor in non-lipid raft regions showed a rapid 20-25% increase in EphA4 activation, whereas the Lyn-EphA4 biosensor showed only a minor FRET change even 10 min after stimulation (Figure 2.5D-E). KRas- or Lyn-EphA4 biosensor with the Y596F or R175V inactivating mutations did not show a FRET response in MEF cells upon ligand stimulation (Figure 2.6). Consistent results were obtained when the biosensor was tested with ephrinA1 stimulation of the HEK293AD-EphA4 system (Figure 2.6). Altogether, the results suggest that the differential FRET responses of KRas-EphA4 and Lyn-EphA4 biosensors are not due to their different membrane targeting tags, but they rather reflect the differential localization of activated EphA4 in response to ephrin ligands in specific membrane microdomains. In particular, the results indicate a faster and stronger EphA4 activation in non-raft region than in raft-like microdomains.

2.4.4 Cytoskeleton regulation is involved in differential EphA4 activation at different compartments of plasma membrane

The plasma membrane is directly connected with and supported by cytoskeletal structures, including polymerized actin and microtubule filaments (27). Actin filaments interact with raft-like microdomains through proteins such as annexins and polybasic proteins (17). Therefore, in order to investigate the downstream mechanisms responsible for the differential EphA4 activation patterns in different plasma membrane microdomains, we examined the role of the actin cytoskeleton.

MEF cells were pretreated with cytochalasin D (cytoD) for 1 hr to block actin polymerization. Interestingly, upon ephrinA1 stimulation of cells treated with cytoD, the KRas-EphA4 biosensor in non-lipid raft regions still showed 20-25% increase in the ECFP/YPet ratio, whereas the Lyn-EphA4 biosensor had a much increased response with a 35-40% change in FRET signal (Figure 2.7). These results suggest that actin filaments, which connect to raft-like microdomains, inhibit EphA4 receptor activation by ephrin ligands.

2.5 Discussions

EphA4 functions are closely dependent on the subcellular localization of the receptor. However, it remains unclear how EphA4 activation is regulated in different membrane microdomains. In this study, we developed a FRET based EphA4 biosensor capable of monitoring EphA4 phosphorylation of the Tyr596 motif (found in the EphA4 JM segment) and its subsequent intramolecular binding to the Src SH2 domain. Our

EphA4 biosensor has several advantages for studying signaling hierarchy in single live cells. First, the substrate peptide in the EphA4 biosensor encompasses Tyr596, which can be specifically phosphorylated by EphA4 but not as much by other tyrosine kinases abundant at the plasma membrane such as Src or the PDGFR. In addition, the biosensor mimics the molecular events of EphA4 activation to detect receptor activity, but does not contain the EphA4 kinase domain, which may perturb the endogenous signaling and physiology in live cells. Therefore, the EphA4 FRET biosensor should enable us to monitor EphA4 activity with minimal perturbation of host cells. Finally, EphA4 biosensors with Lyn- and KRas tags are ideal for visualizing local EphA4 activity at dynamic membrane microdomains in live cells with high accuracy.

We observed stronger FRET responses of the non-raft targeting EphA4 biosensor in response to ligand stimulation, while the raft-targeting EphA4 biosensor showed minor activation. However, when we blocked the polymerization of actin filaments, which interact with raft-like domains, EphA4 activation at the raft-like regions significantly increased. This activation pattern may be explained by the fact that raft-like microdomains are known to be more rigid and less fluid than non-raft region (28). Since EphA4 activation requires receptor molecules to cluster upon ligand binding, a more fluid membrane structure in the non-raft region may allow and in fact facilitate the clustering event. Actin filaments have been proposed to anchor raft-like microdomains to regulate lateral diffusion of proteins on the membrane (29). It is hence likely that the interaction between actin filaments and raft-like microdomains could inhibit clustering of EphA4 molecules by raft-associated proteins.

In summary, we have developed a novel FRET-based EphA4 biosensor that allows the detection of EphA4 activity with high spatial and temporal resolution in live cells. Targeting of the EphA4 biosensor to specific membrane microdomains through acylation and prenylation further provides powerful tools to monitor the dynamic molecular activities of EphA4 in specific subcellular compartments. Our results suggest that EphA4 can be activated in different membrane microdomains with distinct kinetics in response to physiological stimulations.

2.6 Acknowledgements

Chapter 2, is nearly identical to a submitted article entitled "A genetically encoded FRET biosensor for visualizing EphA4 activity in different compartments of the plasma membrane" by Pan Y., Lu S., Lei L., Lamberto I., Wang Yi., Pasquale E.B., & Wang Y. The dissertation author was the primary investigator and author of this paper. The authors acknowledge the funding source NIH CA204704, NSF/NIH Math/Bio Initiative DMS-1361421 (S.L. and Y.W.), NIH HL121365, GM125379, CA209629, NSF CBET1360341 (Y. Wang) and NIH NS087070 (E.B.P.).

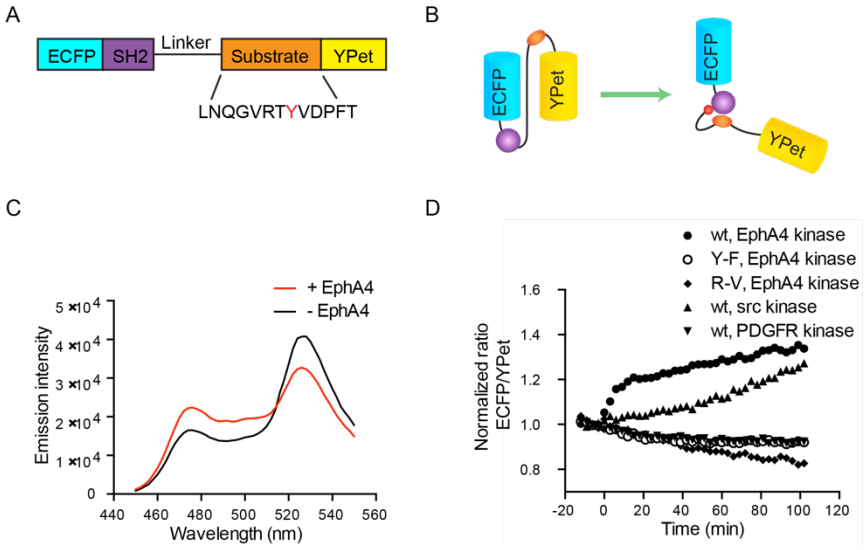

Figure 2.1 The design of the FRET-based EphA4 biosensor and in vitro characterization

(A) The design principle of the EphA4 biosensor. Active EphA4 can phosphorylate the substrate peptide in the EphA4 biosensor, which subsequently binds to the intramolecular SH2 domain to cause a FRET decrease. (B) The EphA4 biosensor is composed of ECFP, the SH2 domain derived from c-Src, a flexible linker, the EphA4 substrate peptide containing Tyr596 (indicated as red Y) and YPet. (C) Emission spectra of the purified EphA4 biosensor before (black) and after (red) the phosphorylation by EphA4 for 2 h. (D) The time courses of the ECFP/YPet emission ratio of the EphA4 biosensor (1 μM) before and after incubation with EphA4 (1 μg/ml), Src kinase (1 μg/ml) or PDGFR (1 μg/ml) (n = 3). The time course of EphA4 YF mutant biosensor (1 μM) before and after EphA4 stimulation was also shown (n = 3). The ECFP/YPet ratios were normalized against the averaged values before enzyme incubation.

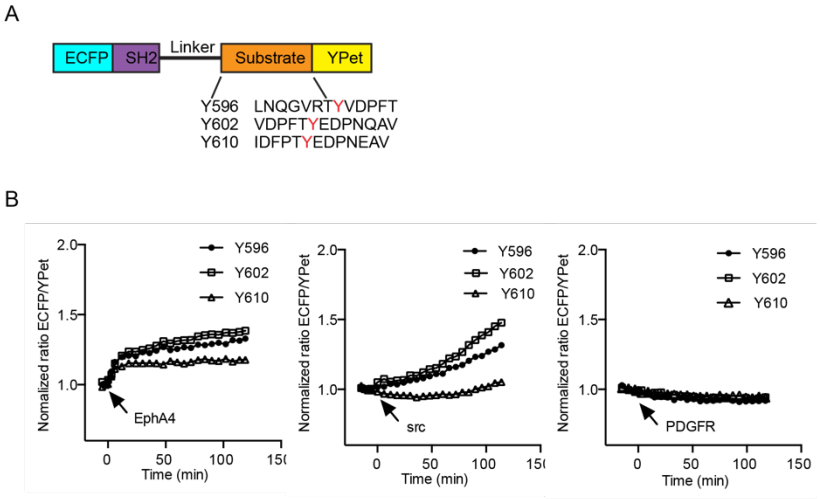

Figure 2.2 The FRET response of EphA4 biosensor in mammalian cells.

(A) The cartoon showing the design of three EphA4 biosensor candidates with different substrate peptide sequences. Candidates substrates Y596, Y602 were derived from EphA4 juxtamembrane (JM) region, Y610 was derived from EphB2 JM region. (B) The representative time courses of the ECFP/YPet emission ratio of the purified EphA4 biosensor candidates Y596 (black square), Y602 (white square), and Y610 (triangle) on EphA4 kinase (left panel), Src kinase (middle panel), or PDGFR (right panel) stimulation.

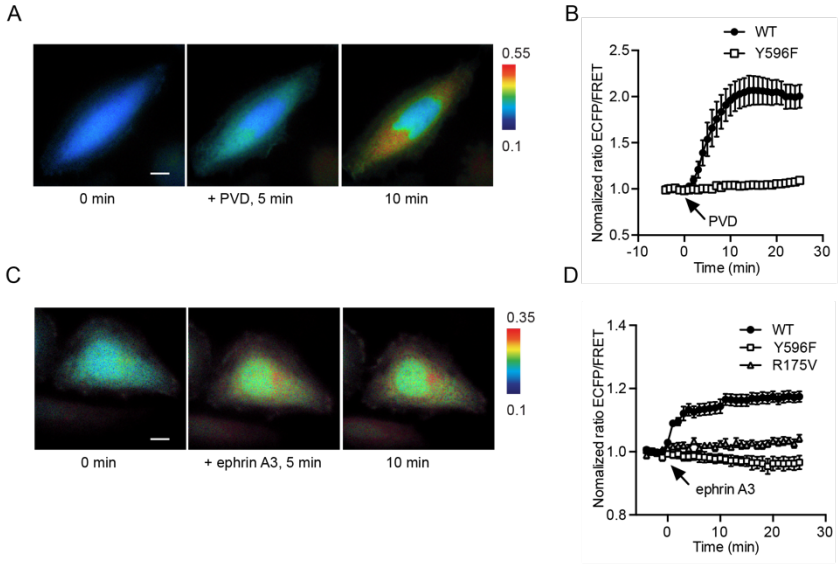

Figure 2.3 Characterization of EphA4 biosensor candidates.

(A) The representative ECFP/YPet ratio images of the EphA4 biosensor in HeLa cells before and after PVD stimulation (Scale bar, 10 μm). (B) The time coursess of normalized ECFP/YPet ratio (Mean ± SEM) of EphA4 (n = 12) or Y596F (n = 7) mutant biosensor before and after PVD stimulation in HeLa cells. (C) The representative ECFP/YPet ratio images of the EphA4 biosensor in HeLa cells before and after ephrinA3 stimulation (Scale bar, 10 μm). (D) The time course of normalized ECFP/YPet ratio (Mean ± SEM) of EphA4 (black square, n = 21) or Y596F (white square, n = 6), R175V (triangle, n = 9) mutant biosensors before and after PVD stimulation in HeLa cells.

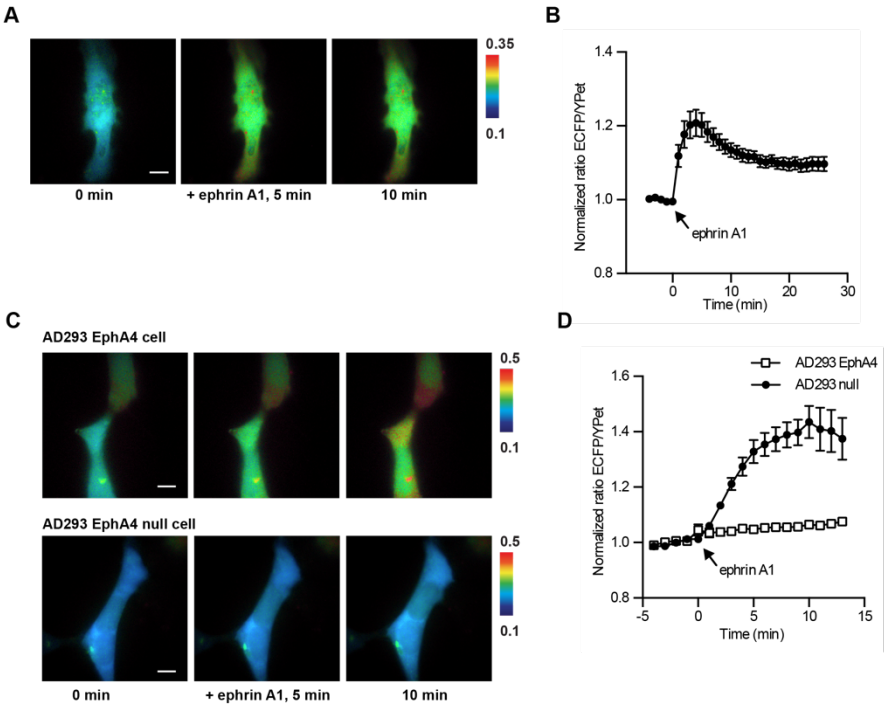

Figure 2.4 FRET response for the EphA4 biosensor in HeLa and HEK293AD-EphA4 cells.

(A) Representative images of the ECFP/YPet ratios for the EphA4 biosensor in HeLa cells before and after ephrinA1 stimulation (scale bar, 10 μm). (B) Time course of normalized ECFP/YPet ratios (mean ± SEM) the for the cytoplasmic EphA4 biosensor (n = 13) before and after ephrinA1 stimulation in HeLa cells. (C) Representative images for the ECFP/YPet ratios of the cytoplasmic EphA4 biosensor in HEK293AD-EphA4 cells (top panel) or EphA4 null cells (bottom panel) before and after PVD stimulation (Scale bar, 10 μm). (D) Time course of normalized ECFP/YPet ratios (mean ± SEM) for the EphA4 biosensor in HEK293AD-EphA4 cells (n = 11) or EphA4 null control cells (n = 9) mutant biosensor before and after ephrinA1 ligand stimulation.

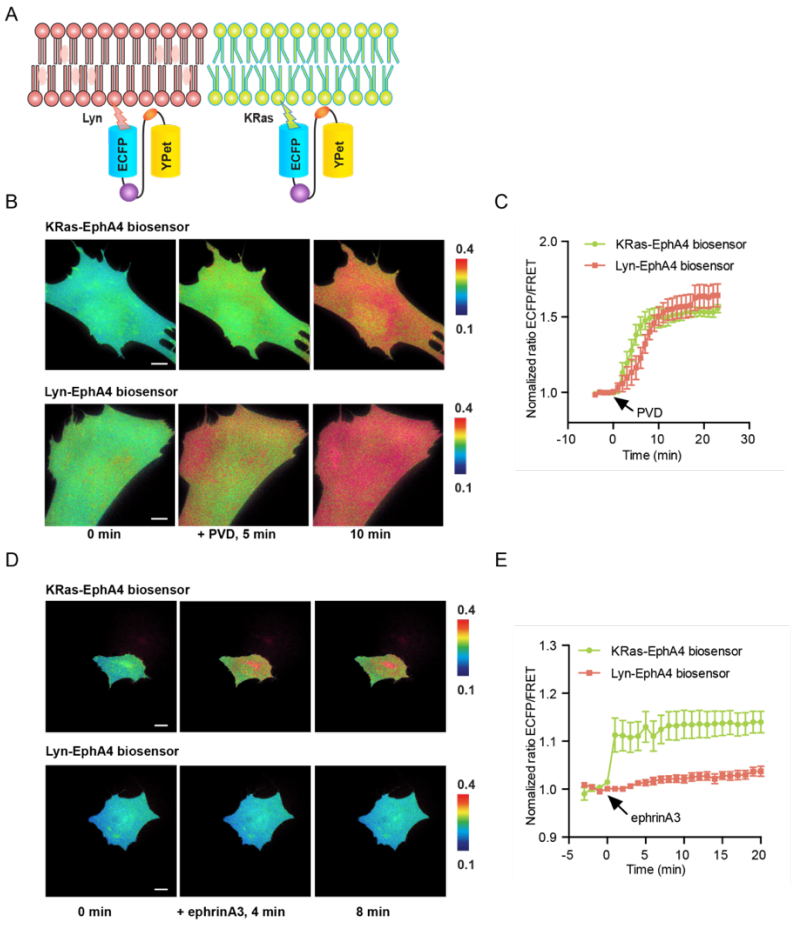

Figure 2.5 EphA4 activation in raft-like domains and non-lipid rafts

(A) The design principle of non-lipid raft targeted (KRas-EphA4) and lipid raft targeted (Lyn-EphA4) biosensors. The KRas biosensor was constructed by fusing a polybasic-geranylgeranyl motif (cysteine) adapted from K-Ras to the C-terminus of the cytosolic EphA4 (cyto-EphA4) biosensor. The Lyn-EphA4 biosensor was constructed by fusing a lipid raft targeting motif containing myristoylation and palmitoylation sites (glycine and cysteine) derived from Lyn to the N-terminus of the cytosolic EphA4 (Cyto-EphA4) biosensor. (B) The representative ECFP/YPet ratio images KRas-EphA4 biosensor and Lyn-EphA4 biosensor in HeLa cells before and after PVD stimulation (Scale bar, 10 μm). (C) The time courses of normalized ECFP/YPet ratio (Mean ± SEM) of KRas-EphA4 biosensor (green line, n = 10) and Lyn-EphA4 biosensor (red line, n = 6) before and after PVD stimulation in HeLa cells. (D) The representative ECFP/YPet ratio images KRas-EphA4 biosensor and Lyn-EphA4 biosensors in HeLa cells before and after ephrinA3 stimulation (Scale bar, 10 μm). (E) The time courses of normalized ECFP/YPet ratio (Mean ± SEM) of KRas-EphA4 biosensor (green line, n = 16) and Lyn-EphA4 biosensor (red line, n = 14) before and after ephrinA3 stimulation in HeLa cells.

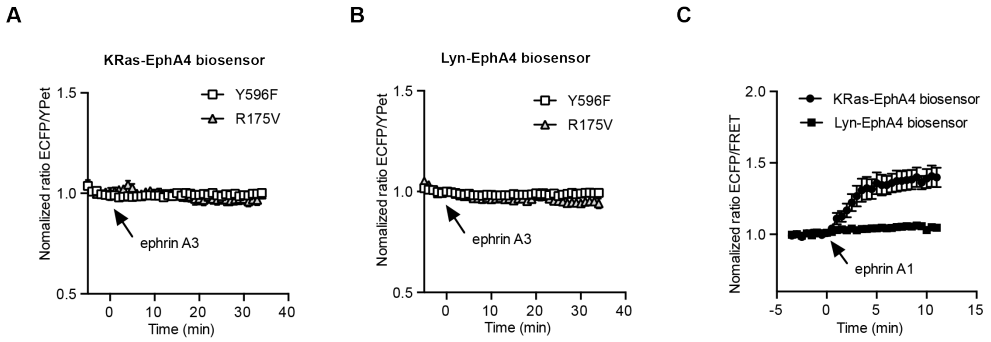

Figure 2.6 FRET responses for the membrane-targeted EphA4 biosensors in MEF and HEK293AD-EphA4 cells

(A) Time course of the normalized ECFP/YPet ratios (Mean ± SEM) for the KRas-EphA4 biosensor Y596F mutant (square, n = 6) and R175V mutant (triangle, n = 6) before and after ephrinA3 stimulation in HeLa cells. (A) Time course of the normalized ECFP/YPet ratios for the Lyn-EphA4 biosensor Y696F mutant (square, n = 8) and the R175V mutant (triangle, n = 5) before and after ephrinA3 stimulation in MEF cells. (C) Time course of normalized the ECFP/YPet ratios (mean ± SEM) for the KRas-EphA4 (circle, n = 7) and Lyn-EphA4 (square, n = 10) biosensors before and after ephrinA1 stimulation in HEK293AD-EphA4 cell lines.

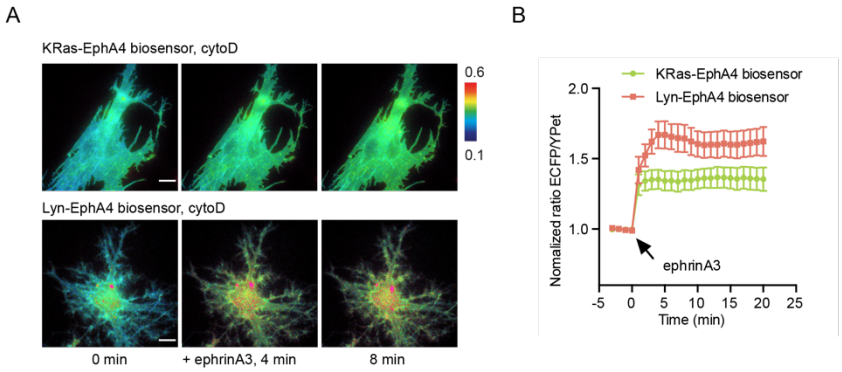

Figure 2.7 Actin filaments differentially regulates EphA4 activation at plasma membrane

(A)The representative ECFP/YPet ratio images KRas-EphA4 biosensor and Lyn-EphA4 biosensor in cytochalasin D (cytoD) pretreated HeLa cells before and after ephrinA3 stimulation (Scale bar, 10 μm). (B) The time courses of normalized ECFP/YPet ratio (Mean ± SEM) of KRas-EphA4 biosensor (green line, n = 10) and Lyn-EphA4 biosensor (red line, n = 6) before and after ephrinA3 stimulation in CytoD pretreated HeLa cells.

2.7 References

1. Gale NW, Holland SJ, Valenzuela DM, Flenniken A, Pan L, Ryan TE, Henkemeyer M, Strebhardt K, Hirai H, Wilkinson DG, Pawson T, Davis S, & Yancopoulos GD (1996) Eph receptors and ligands comprise two major specificity subclasses and are reciprocally compartmentalized during embryogenesis. *Neuron* 17(1):9-19.

2. Pasquale EB (2008) Eph-ephrin bidirectional signaling in physiology and disease. *Cell* 133(1):38-52.

3. Klein R (2012) Eph/ephrin signalling during development. *Development* 139(22):4105-4109.

4. Flanagan JG & Vanderhaeghen P (1998) The ephrins and Eph receptors in neural development. *Annu Rev Neurosci* 21:309-345.

5. Egea J, Nissen UV, Dufour A, Sahin M, Greer P, Kullander K, Mrsic-Flogel TD, Greenberg ME, Kiehn O, Vanderhaeghen P, & Klein R (2005) Regulation of EphA4 kinase activity is required for a subset of axon guidance decisions suggesting a key role for receptor clustering in Eph function. *Neuron* 47(4):515-528.

6. Surawska H, Ma PC, & Salgia R (2004) The role of ephrins and Eph receptors in cancer. *Cytokine Growth F R* 15(6):419-433.

7. Pasquale EB (2010) Eph receptors and ephrins in cancer: bidirectional signalling and beyond. *Nat Rev Cancer* 10(3):165-180.

8. Fox BP & Kandpal RP (2004) Invasiveness of breast carcinoma cells and transcript profile: Eph receptors and ephrin ligands as molecular markers of potential diagnostic and prognostic application. *Biochem Bioph Res Co* 318(4):882-892.

9. Saintigny P, Peng SH, Zhang L, Sen B, Wistuba II, Lippman SM, Girard L, Minna JD, Heymach JV, & Johnson FM (2012) Global Evaluation of Eph Receptors and Ephrins in Lung Adenocarcinomas Identifies EphA4 as an Inhibitor of Cell Migration and Invasion. *Mol Cancer Ther* 11(9):2021-2032.

10. Fukai J, Yokote H, Yamanaka R, Arao T, Nishio K, & Itakura T (2008) EphA4 promotes cell proliferation and migration through a novel EphA4-FGFR1 signaling pathway in the human glioma U251 cell line. *Mol Cancer Ther* 7(9):2768-2778.

11. Hachim IY, Villatoro M, Canaff L, Hachim MY, Boudreault J, Haiub H, Ali S, & Lebrun JJ (2017) Transforming Growth Factor-beta Regulation of Ephrin Type-A Receptor 4 Signaling in Breast Cancer Cellular Migration. *Sci Rep-Uk* 7.

12. Davis S, Gale NW, Aldrich TH, Maisonpierre PC, Lhotak V, Pawson T, Goldfarb M, & Yancopoulos GD (1994) Ligands for EPH-related receptor tyrosine kinases that require membrane attachment or clustering for activity. *Science* 266(5186):816-819.

13. Kania A & Klein R (2016) Mechanisms of ephrin-Eph signalling in development, physiology and disease. *Nat Rev Mol Cell Bio* 17(4):240-256.

14. Klausner RD, Kleinfeld AM, Hoover RL, & Karnovsky MJ (1980) Lipid domains in membranes. Evidence derived from structural perturbations induced by free fatty acids and lifetime heterogeneity analysis. *J Biol Chem* 255(4):1286-1295.

15. Pike LJ (2006) Rafts defined: a report on the Keystone Symposium on Lipid Rafts and Cell Function. *J Lipid Res* 47(7):1597-1598.

16. Jacobson K, Mouritsen OG, & Anderson RGW (2007) Lipid rafts: at a crossroad between cell biology and physics. *Nat Cell Biol* 9(1):7-14.

17. Edidin M (2003) The state of lipid rafts: from model membranes to cells. *Annu Rev Biophys Biomol Struct* 32:257-283.

18. Yumoto N, Wakatsuki S, Kurisaki T, Hara Y, Osumi N, Frisen J, & Sehara-Fujisawa A (2008) Meltrin beta/ADAM19 interacting with EphA4 in developing neural cells participates in formation of the neuromuscular junction. *PLoS One* 3(10):e3322.

19. Chichili GR & Rodgers W (2009) Cytoskeleton-membrane interactions in membrane raft structure. *Cell Mol Life Sci* 66(14):2319-2328.

20. Ouyang M, Sun J, Chien S, & Wang Y (2008) Determination of hierarchical relationship of Src and Rac at subcellular locations with FRET biosensors. *Proc Natl Acad Sci U S A* 105(38):14353-14358.

21. Zacharias DA, Violin JD, Newton AC, & Tsien RY (2002) Partitioning of lipid-modified monomeric GFPs into membrane microdomains of live cells. *Science* 296(5569):913-916.

22. Huyer G, Liu S, Kelly J, Moffat J, Payette P, Kennedy B, Tsaprailis G, Gresser MJ, & Ramachandran C (1997) Mechanism of inhibition of protein-tyrosine phosphatases by vanadate and pervanadate. *J Biol Chem* 272(2):843-851.

23. Wang Y, Botvinick EL, Zhao Y, Berns MW, Usami S, Tsien RY, & Chien S (2005) Visualizing the mechanical activation of Src. *Nature* 434(7036):1040-1045.

24. Warner N, Wybenga-Groot LE, & Pawson T (2008) Analysis of EphA4 receptor tyrosine kinase substrate specificity using peptide-based arrays. *FEBS J* 275(10):2561-2573.

25. Wimmer-Kleikamp SH, Janes PW, Squire A, Bastiaens PI, & Lackmann M (2004) Recruitment of Eph receptors into signaling clusters does not require ephrin contact. *J Cell Biol* 164(5):661-666.

26. Winter J, Roepcke S, Krause S, Muller EC, Otto A, Vingron M, & Schweiger S (2008) Comparative 3'UTR analysis allows identification of regulatory clusters that drive Eph/ephrin expression in cancer cell lines. *PLoS One* 3(7):e2780.

27. Fletcher DA & Mullins RD (2010) Cell mechanics and the cytoskeleton. *Nature* 463(7280):485-492.

28. Gallegos AM, McIntosh AL, Atshaves BP, & Schroeder F (2004) Structure and cholesterol domain dynamics of an enriched caveolae/raft isolate. *Biochem J* 382(Pt 2):451-461.

29. Head BP, Patel HH, & Insel PA (2014) Interaction of membrane/lipid rafts with the cytoskeleton: impact on signaling and function: membrane/lipid rafts, mediators of cytoskeletal arrangement and cell signaling. *Biochim Biophys Acta* 1838(2):532-545.

Chapter 3 The development of Laser induced shockwave (LIS) for activation of Piezo1 ion channel

3.1 Abstract

Piezo1 belongs to mechano-activatable cation channels serving as biological pressure sensors. However, the molecular hierarchy downstream of Piezo1 activation remains unclear. In this study, we used biosensors based on fluorescence resonance energy transfer (FRET) to demonstrate that laser-induced shockwaves (LIS) can mechanically activate Piezo1 to induce a transient intracellular calcium ($Ca_{[i]}$) elevation, accompanied by FAK activation. Tuning the degree of Piezo1 activation by chemical stimuli, by titrating either the dosage of Piezo1 ligand Yoda1 or the expression level of Piezo1, revealed a bimodal pattern of Piezo1 actions on downstream molecular events. A low degree of Piezo1 activation (transient mode) leads to a transient $Ca_{[i]}$ response with FAK activation, whereas a high degree of Piezo1 activation (sustained mode) causes a sustained $Ca_{[i]}$ response with FAK suppression. These results suggest that LIS can specifically trigger the transient activation mode of Piezo1 to result in a transient $Ca_{[i]}$ response and a FAK activation.

3.2 Introduction

Cells constantly encounter physical forces in the forms of shear stress, compression and stretching. Mechanotransduction is crucial for cells to perceive the local microenvironments in order to maintain cellular function and tissue homeostasis (1-4). Alterations of mechanotransduction can lead to pathological conditions (5). It remains unclear, however, on the detailed mechanism by which cells perceive these mechanical cues of the external microenvironment and transduce them into molecular signals and genetic regulations for the coordination of cellular responses.

Several families of molecular mechanoreceptors have been reported to transduce mechanical stimulation into ion currents to modulate physiological functions, particularly the transmembrane ion channel proteins (6). Piezo1 has been identified as a component of mechanically activated cation channels in both vertebrates and non-vertebrates. It induces currents in various cell types upon the application of mechanical pressure to the cell membrane (7, 8). Consequently, Piezo1 plays an important role in physiology, including angiogenesis, vasculogenesis (9), and erythrocyte volume regulation (10). Piezo1 is also involved in regulating cancer biology. For instance, blocking Piezo1 decreased the motility of the breast cancer cell line MCF-7 (11), but increased the migration speed of small cell lung cancer cell lines (12). These results suggest a complex role of Piezo1 in regulating cancer cell migration under different biological and environmental contexts, which remains to be elucidated.

In this study, we applied laser-induced shockwaves (LIS) to activate the Piezo1 in live cells and studied the mechanism by which Piezo1 regulates molecular events,

e.g. intracellular calcium ($Ca_{[i]}$) and the activity of focal adhesion kinase (FAK). LIS are produced by the sudden buildup of energy at the focus of a short-pulsed laser beam (13). The subsequent microplasma cavitation, followed by microbubble expansion and contraction, can exert a large mechanical force in the surrounding area (14). The force is controllable in magnitude by tuning the laser power and can exert instantaneous pressures at the MegaPascal range. Therefore, LIS can serve as a mechanical stimulator of Piezo1 on single live cells with high precision in space and time (15). Genetically encoded biosensors based on FRET have enabled the visualization of signaling events in live cells with high spatio-temporal resolution (16). They can be applied at the same time to monitor in live cells the Piezo1 activation and its associated $Ca_{[i]}$ dynamics, as well as the FAK activation, a crucial signaling component that regulates cell adhesion and motility (17). Our results revealed a bimodal pattern of Piezo1 action on $Ca_{[i]}$ dynamics (transient vs. sustained) and downstream FAK molecular events (activation vs. inhibition), with the mechanical force exerted by LIS specifically eliciting the transient mode of Piezo1 actions. These results advance our understanding of Piezo1 activation and its role in perceiving mechanical cues and regulating intracellular molecular signals.

3.3 Materials and Methods

3.3.1 DNA plasmid

The construct of the mPiezo1-tdTomato was obtained from Dr. Patapoutian's lab (10). The D3cpv calcium FRET biosensor was previously described (18), the cytosolic FAK FRET biosensor was previously developed and described (19).

3.3.2 Cell culture and transfection

HeLa cells were purchased from ATCC. HEK 293T cell line was a kind gift from Dr. Patapoutian's lab (7). Cell culture reagents were obtained from Invitrogen. Cells were maintained in Dulbecco's modified Eagle medium (DMEM) supplemented with 10% fetal bovine serum (FBS), 2 mM L-glutamine, 1 unit/ml penicillin, 100 μg/ml streptomycin, and 1 mM sodium pyruvate. Cells were cultured in a humidified 95% air, 5% CO_2 incubator at 37 °C. FUGENE 6 (Invitrogen) was used for transfection of DNA plasmids. Cells were tested 36-48 hr post transfection.

During imaging, cells were cultured in fibronectin coated cover-glass-bottom dishes and maintained in Hanks Buffered Saline solution (HBSS) with or without Calcium and Magnesium (Invitrogen, Carlsbad, CA). Chemical stimulant, Yoda1, was purchased from Thermo fisher scientific.

3.3.3 Laser-Shockwave System

The laser used for the shockwave stimulation is a 532 nm wavelength, 100 Hz repetition rate, 2 ns pulse width Coherent Flare system (Spectra-Physics). Laser power is attenuated by rotating an optical polarizer mounted in a stepper-motor-controlled rotating mount (New Port). A mechanical shutter (Vincent Associates) with a 10-15 ms

duty cycle is gated to allow 1-2 laser pulses to pass through when firing. The beam expanders are used to adjust the beam diameter of the lasers to fill the back aperture of the objective. The custom laser entry port (CLEP) is placed underneath the objective (phase III, 40x, NA 1.3, oil immersion) of a Zeiss Axiovert 200M microscope. The filter on the CLEP was chosen to direct the laser lights onto the lower right corner of the image screen.

3.3.4 Laser-induced shockwave (LIS)

In order to understand precisely the forces presented in the shockwave system, we followed a similar method in a previous publication to measure and calculate forces (14). The time resolved shockwave signal was determined by monitoring the size of each bubble created by the shockwave. In order to achieve this, a low power measurement laser at 633 nm was arranged to be coaxial with the shockwave beam. The transmitted power of the beam was monitored using a fast photodiode. Upon the creation of a bubble during the measurement, laser was turned off and the signal was captured.

A series of measurements at different powers between time-averaged 160 μW and 293 μW measured at the back aperture were conducted. The peak beam deflection and the time of bubble rise and collapse were recorded for calculation.

By utilizing the Rayleigh Equation for bubble growth:

$$R_{max} = \frac{T}{0.915}\left[\frac{p_\infty - p_v}{\rho}\right]^{\frac{1}{2}}$$

Where R_{max} is the maximum bubble radius, T is the time for bubble collapse. Here p_∞ is the atmospheric pressure, $p_v$is the vapor pressure within the bubble and ρ is the density of the fluid. This information can then be fit into the Gilmore Equation and applied to a Logarithmic fit function to calculate the time dependent bubble expansions.

The radial shear forces can then be calculated by applying the methods shown previously (13)

Table 3.1 The radial distribution of shear forces.

Time averaged power	*Optical intensity (W/m)*	*Pulse Energy (μJ)*	*Bubble Energy (μJ)*	*Peak Shear Stress (MPa)*
164 μW	1.2442e+13	1.6	0.12	21.1
170 μW	1.2897e+13	1.7	0.22	21.3
180 μW	1.3656e+13	1.8	0.23	21.8

We noted that cells have been shown to survive through pressures up to 120 MPa (20), as cell lysis is not only dependent on the peak shear but also on the duration of the applied shear stress, as well as cell types and bubble expansion radius. The cell lysis was observed to occur at distances below 120 μm away from the epicenter of the cavitation with our current experimental configuration. In our mechano-stimulation experiments, cells were positioned more than 190 μm away from the cavitation epicenter to avoid cell damages.

3.3.5 Image acquisition

Images of shockwave stimulation were collected by ORCA-Flash4.0 V2 Digital CMOS camera (Hamamatsu) passing a 440DF20 excitation filter, a 455DRLP dichroic

mirror, and two emission filters placed in a dual view adaptor (480DF30 for ECFP and 535DF25 for EYFP). Images of agonist stimulation were collected from a Nikon microscope with a charge-coupled device (CCD) camera with the same filter setting. For FAK biosensor, the pixel-by-pixel ratio images of ECFP/FRET were calculated based on the background-subtracted fluorescence intensity images of CFP and YFP by the Metafluor program to allow quantification and statistical analysis of FRET responses. For calcium biosensor, the emission ratio of FRET/ECFP was used to represent calcium activity. The emission ratio images were shown in the intensity modified display (IMD) mode.

3.4 Results

To explore whether LIS-induced mechanical stimulation can activate the Piezo1 channel, HEK 293T cells co-transfected with Piezo1-tdTomato and a CFP/YFP-based FRET calcium biosensor (18) were examined in a LIS-FRET imaging system (21) (Figure 3.1).

Upon LIS stimulation of the Piezo1-expressing HEK cells, calcium influx was immediately detected in cells cultured in calcium-containing HBSS media, but not in HBSS without calcium. In control HEK cells transfected only with a calcium biosensor but not Piezo1, there was no significant calcium influx in HBSS media with or without calcium (Figure 3.2A-B). In HBSS media without calcium, there was a very minor calcium increase in the Piezo1-transfected cells (Figure 3.2B), possibly due to the ER calcium release since Piezo1 can be expressed in ER (12). In order to create a shockwave

sufficient to mechanically stimulate the target cells (14) without inducing damage, laser power was precisely controlled in a range between 160 and 180 μW (Figure 3.3). Indeed, intermittent shockwave pulses could elicit multiple calcium waves (Figure 3.3C), verifying a healthy response and a lack of shockwave-induced damage on the target cell. We have also examined Piezo1 in HeLa cells expressing low levels of endogenous Piezo1 (Figure 3.5). A Piezo1-dependent calcium influx was clearly observed, suggesting that LIS can activate Piezo1 to trigger transient $Ca_{[i]}$ dynamics in different cell types.

We next examined the effect of LIS on FAK activity visualized by a FAK FRET biosensor developed earlier by us (19). HEK 293T cells co-transfected with Piezo1-tdTomato and the CFP/YFP-based FAK FRET biosensor were exposed to LIS in HBSS media containing calcium. Shockwave stimulation caused an increase of FAK activity in HEK cells transfected with Piezo1, but no significant change in the control HEK cells without Piezo1 expression (Figure 3.4). These results indicate that LIS-induced Piezo1 activation could lead to FAK activation, potentially due to the transient calcium influx.

Aside from mechanical stimulation, chemical agonists can also activate the Piezo1 ion channel. To further gain molecular insights on the role of Piezo1 in FAK activation, Yoda1, a synthetic small molecule that has been reported to act as a specific agonist for activating human and mouse Piezo1 (22), was applied to stimulate Piezo1. We stimulated HEK cells that have been co-transfected with Piezo1 and the FAK FRET biosensor with 25 μM Yoda1 as a standard dosage (22). Surprisingly, Yoda1 stimulation of Piezo1 caused a significant decrease of FAK activity in the HEK cells expressing

exogenous Piezo1 (Figure 3.6A-B); this is opposite to the increase in FAK activity in response to mechanical stimulation of Piezo1 by LIS. It was hence hypothesized that the LIS-induced mechanical and Yoda1-based chemical stimulations result in different modes of the Piezo1 activation. To test this hypothesis, we co-transfected HEK cells with Piezo1 and the calcium FRET biosensor. Upon Yoda1 stimulation at 25 μM, a sustained calcium influx was observed in the HEK cells transfected with Piezo1 (Figure 3.6C-D). This is significantly different from the transient $Ca_{[i]}$ dynamics observed in LIS stimulated cells (Figure 3.2A). The difference in the patterns of $Ca_{[i]}$ dynamics upon mechanical and chemical stimulations may explain the differential FAK activities in response to these two types of stimuli. To further examine this hypothesis, we titrated the concentration of Yoda1 used to stimulate HEK cells transfected with Piezo1. We observed that a decrease of Yoda1 concentration from 25 to 0.5 μM caused a shift in the pattern of $Ca_{[i]}$ dynamics from a sustained increase to a transient rise (Figure 3.7 and Figure 3.8A-B). Correspondently, the direction of FAK response to Yoda1 stimulation changed from a decrease to an increase when the Yoda1 dosage was reduced from 25 to 0.5 μM in the Piezo1-expressing HEK cells (Figure 3.8C-D). The results of FAK activation induced by both low Yoda1 concentration and LIS-induced FAK activation are accompanied by a transient $Ca_{[i]}$ dynamics. Consistent with these results, increases in the Piezo1 expression level in HEK cells under an intermediate dosage of 2 μM Yoda1 stimulation caused a shift in the dynamic pattern of $Ca_{[i]}$ signaling from transient to sustained (Figure 3.8E). These results suggest that the level of Piezo1 activation led to differential dynamic patterns of calcium influx to result in FAK activation vs.

inhibition. The conclusion derived from studies on HEK cells is supported by our results on HeLa cells, which express endogenous Piezo1 at moderate levels (23). The stimulation in HeLa cells with low level Piezo1 expression by 25 μM Yoda1 caused a transient $Ca_{[i]}$ rise and FAK activation, while introducing high levels of Piezo1 into HeLa cells led to sustained $Ca_{[i]}$ increase and FAK suppression (Figure 3.5).

In summary, our results revealed a bimodal pattern of Piezo1 action on $Ca_{[i]}$ dynamics (transient vs. sustained) and downstream FAK (activation vs. inhibition), with the transient mode causing a transient $Ca_{[i]}$ rise and a FAK activation while the sustained mode causing a sustained $Ca_{[i]}$ rise and a FAK suppression. The mechanical force exerted by LIS can specifically eliciting the transient mode of Piezo1 actions. As such, by combining FRET imaging with laser-based photonics, we have successfully monitored the molecular signaling events with high spatial and temporal resolution in live cells following the mechanosensor Piezo1 activation by LIS mechanical stimulation.

3.5 Discussions

It is interesting that high levels of Piezo1 activation, either attributed to high dosages of Yoda1 application or to high expressions of Piezo1, caused sustained calcium signaling and FAK suppression. Tuning down the Piezo1 activation level can lead to a switch of calcium and FAK responses, with the dynamic $Ca_{[i]}$ signaling

becoming more transient accompanied by an activation of FAK. These results indicate that the strength of Piezo1 activation can lead to two distinctive activation patterns (bimodal) of downstream signaling, with low levels of Piezo1 activation triggering transient calcium signaling and FAK activation (transient mode) while high levels of Piezo1 activation leading to sustained calcium signaling and FAK suppression (sustained mode) (Figure 3.8F). Our findings of the bimodality of Piezo1 activation hence can shed lights on the mechanisms underlying the opposite effects of Piezo1 knockdown on the migration of two cell lines: a decrease for gastric tumor cell (24), but an increase for lung epithelial cells (12). As such, our results provide a mechanistic explanation of the paradox that the manipulation of Piezo1 under different conditions can lead to differential outcomes in cell migration (11, 25).

We have also demonstrated that the mechanical stimulation induced by LIS can lead to the mechanosensor Piezo1 activation specifically causing a transient calcium influx and a FAK activation (transient mode). This is consistent with previous reports that transient calcium influx could lead to increased FAK phosphorylation (26, 27). These results suggest that the mechanical characteristics of LIS stimulation can determine the activation mode of mechanosensor Piezo1, which can govern the specific downstream signaling events and physiological outcomes.

3.6 Acknowledgements

Chapter 3 is nearly identical to a submitted article entitled “Mechanosensor Piezo1 displays different modes of activation” by Pan Y., Shi L., Gomez-Godinez V.,

Preece D., Woo S., Lu S., Chien S., Berns MW., & Wang Y.. The dissertation author was the primary investigator and author of this paper. The authors thank Dr. Ardem Patapoutian for his generosity in providing materials and advice. These authors acknowledge the funding source NIH GM125379, CA204704, CA209629, and HL121365 (Y. Wang), NSF CBET1360341, DMS1361421 (Y. Wang and S.L.), the Beckman Laser Institute Foundation, AFOSR FA9550-08-1-0284, Air Force Office of Scientific Research under award number FA9550-17-1-0193, Beckman Laser Institute Inc. Foundation (M.W.B.). This research was also supported by National Natural Science Foundation of China, NSFC 11428207 (Y. Wang).

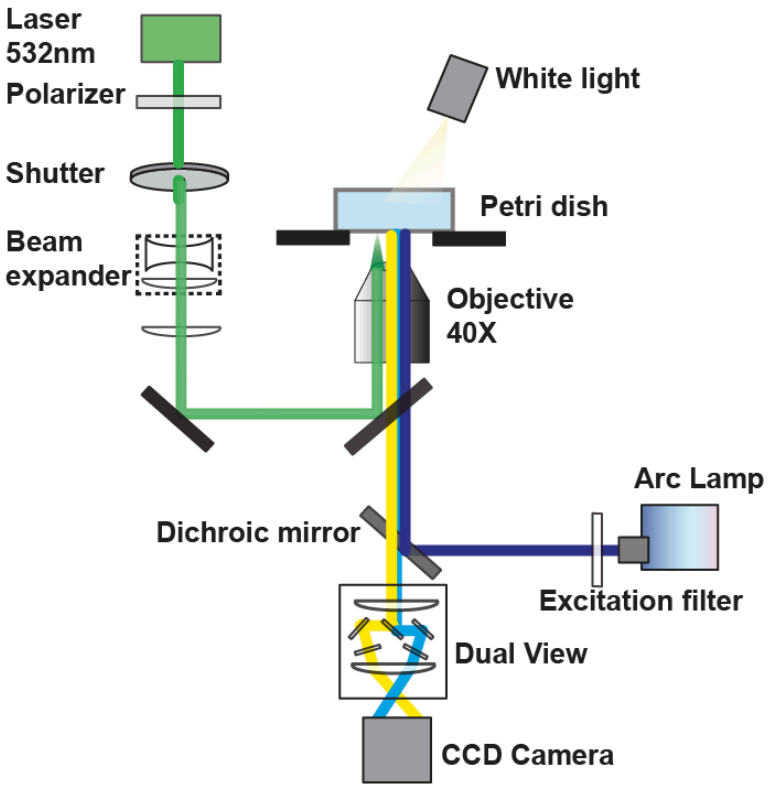

Figure 3.1 Diagram of an integrated system of Laser induced Shockwave (LIS) and FRET imaging

The CCD camera captures fluorescent images of FRET biosensors with 480/30 nm and 535/25 nm bandpass filters integrated in the dual view system. The ablation laser is guided through the side port of the microscope. The arc lamp excitation light enters through the back port of the microscope and is filtered with a 440/20 nm bandpass filter.

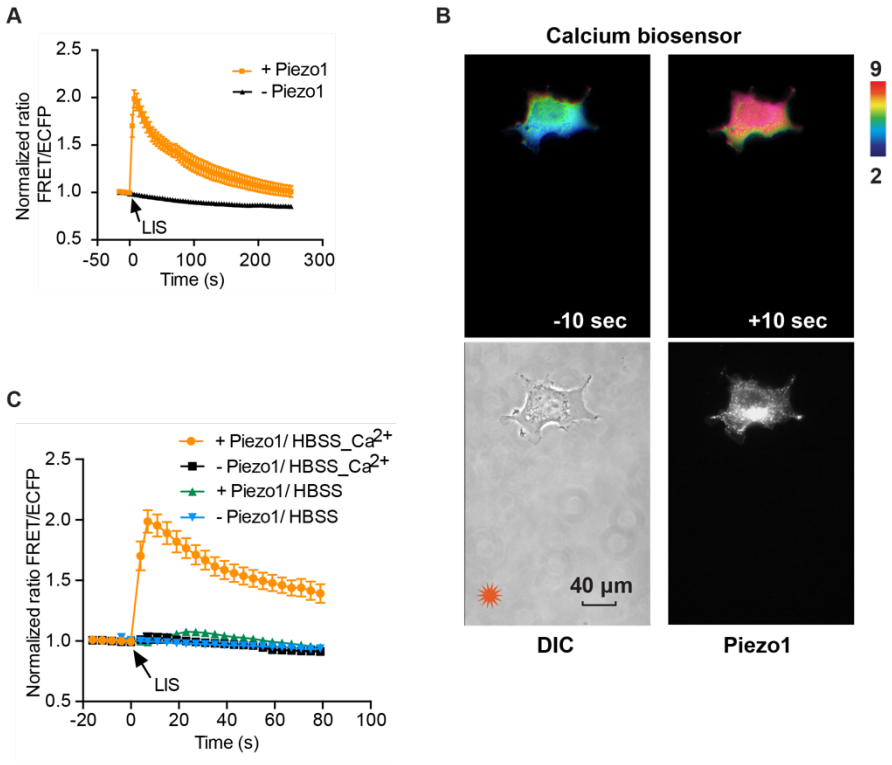

Figure 3.2 The Piezo1 dependent calcium influx upon LIS stimulation in HEK cells

(A) The time courses of normalized FRET ratio (Mean ± SEM) of calcium biosensor before and after shockwave stimulation in HBSS Ca2+ medium with (yellow line, n = 6) or without the Piezo1 expression (black line, n = 6). (B) The representative FRET/ECFP ratio images of calcium biosensor in Piezo1-expressed HEK cells before (top left) and after (top right) LIS stimulation. Phase image with laser initiating point (left) and fluorescent image indicating Piezo1 expression (right) were also shown on the bottom panels (Scale bar, 40 μm). (C) The time courses of normalized FRET/CFP ratio (Mean ± SEM) of d3cpv calcium FRET biosensor before and after shockwave stimulation in HBSS Ca2+ media with (black line, n = 6) or without Piezo1 (orange line, n = 6), or in HBSS only media with (green line, n = 18) or without Piezo1(blue line, n = 14).

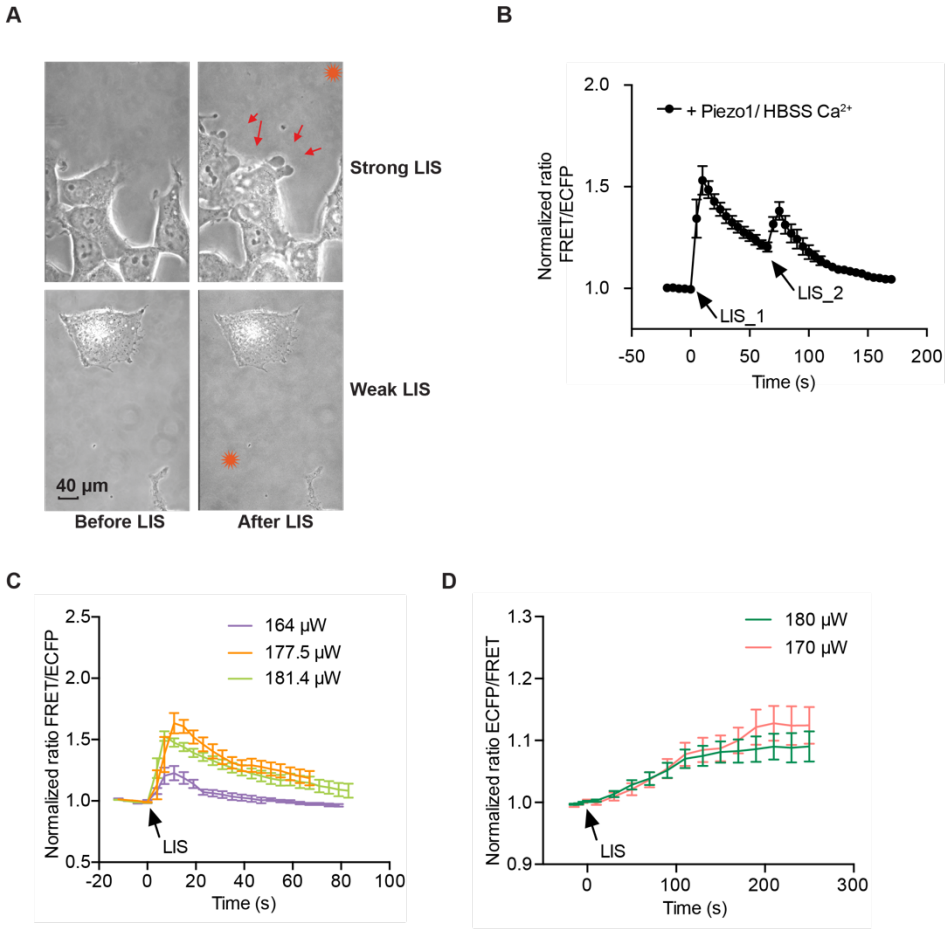

Figure 3.3 Characterization of LIS stimulation on HEK293T cells

(A) Shockwave produced by strong laser power can cause cell damage. The representative phase image of HEK cells before (top left) and after (top right) strong shockwave (200 µW) stimulation. Cells were damaged upon stimulation, as the bubbling indicated by red arrows. The representative DIC images of HEK cells before (bottom left) and after (bottom right) weak shockwave (180 µW) stimulation were shown to indicate that cells were alive and not damaged upon stimulation. (B) The time course of normalized FRET ratio (Mean ± SEM) of calcium biosensor in the Piezo1-expressing HEK cells before and after multiple shockwave stimulations in HBSS Ca2+ medium (n = 6). (C) The time course of normalized FRET ratio (Mean ± SEM) of d3cpv biosensor before and after LIS stimulation at different laser power strengths (purple line, n = 4, yellow line, n = 7, green line, n = 5). (D) The time course of normalized FRET ratio (Mean ± SEM) of FAK biosensor before and after LIS stimulation at different laser power strengths (pink line, n = 8, green line, n = 8).

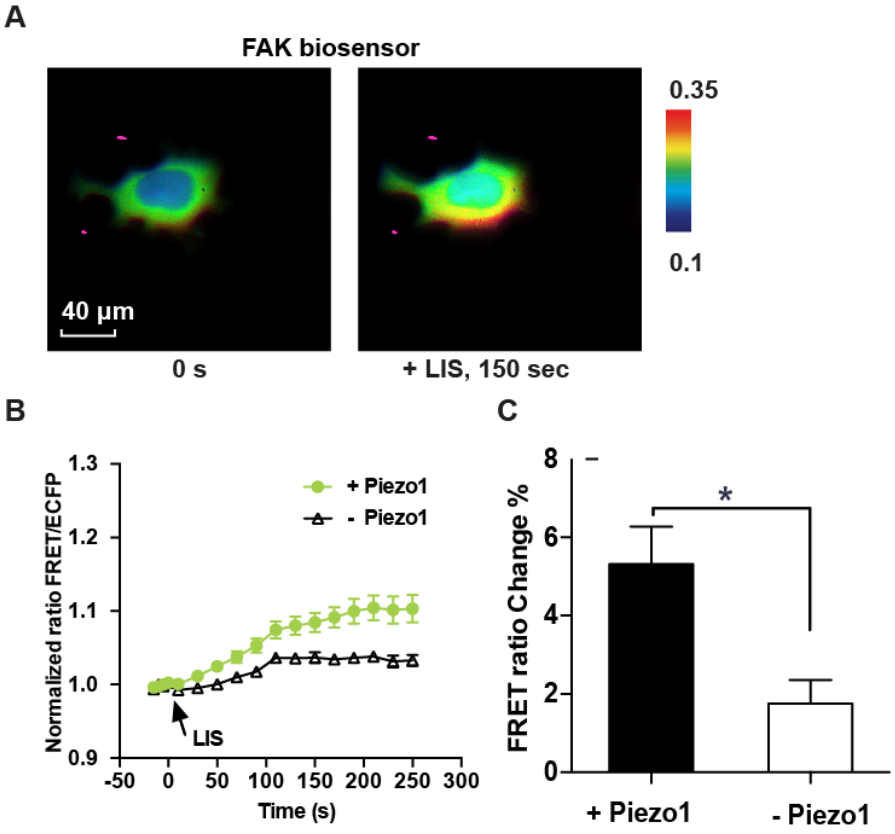

Figure 3.4 The Piezo1-dependent FAK activation upon LIS stimulation in HEK cells

(A) The representative ECFP/FRET ratio images of FAK biosensor in Piezo1 overexpressed HEK cells before (left) and after (right) shockwave stimulation (Scale bar, 40 μm). (B) The time courses of normalized ECFP/FRET ratio (Mean ± SEM) of FAK FRET biosensor before and after shockwave stimulation in HBSS Ca^{2+} media with (green line, n = 16) or without Piezo1 (black line, n = 10). (C) The percentage change of FRET ratio of the FAK FRET biosensor in the Piezo1-expressing HEK cells after shockwave stimulation in HBSS medium with or without calcium. *P < 0.05 from student two-tailed t-test.

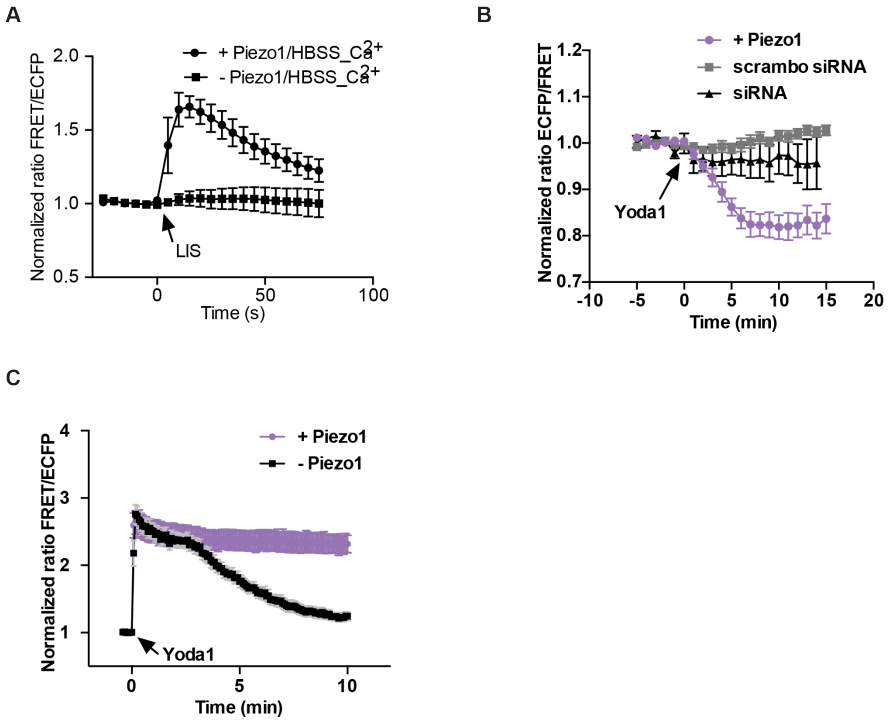

Figure 3.5 The Piezo1-dependent calcium and FAK activation upon LIS stimulation in HeLa cells

(A) Piezo1 dependent calcium influx upon shockwave stimulation in HeLa cells. The time course of normalized FRET/ECFP ratio (Mean ± SEM) of d3cpv biosensor before and after shockwave stimulation in HBSS Ca2+ media with (dot line, n = 4) or without Piezo1(square line, n = 3). (B) The time courses of normalized FRET ratio (Mean ± SEM) of FAK biosensor before and after shockwave stimulation in HeLa cells expressed with high levels of Piezo1 (purple line, n = 3), scramble siRNA (grey line, n = 5), or Piezo1 siRNA to knock down Piezo1 expression (black line, n = 4). (C) The time courses of normalized FRET ratio (Mean ± SEM) of d3cpv calcium biosensor before and after shockwave stimulation in HeLa cells with (purple line, n = 14) or without (black line, n = 16) Piezo1 overexpression.

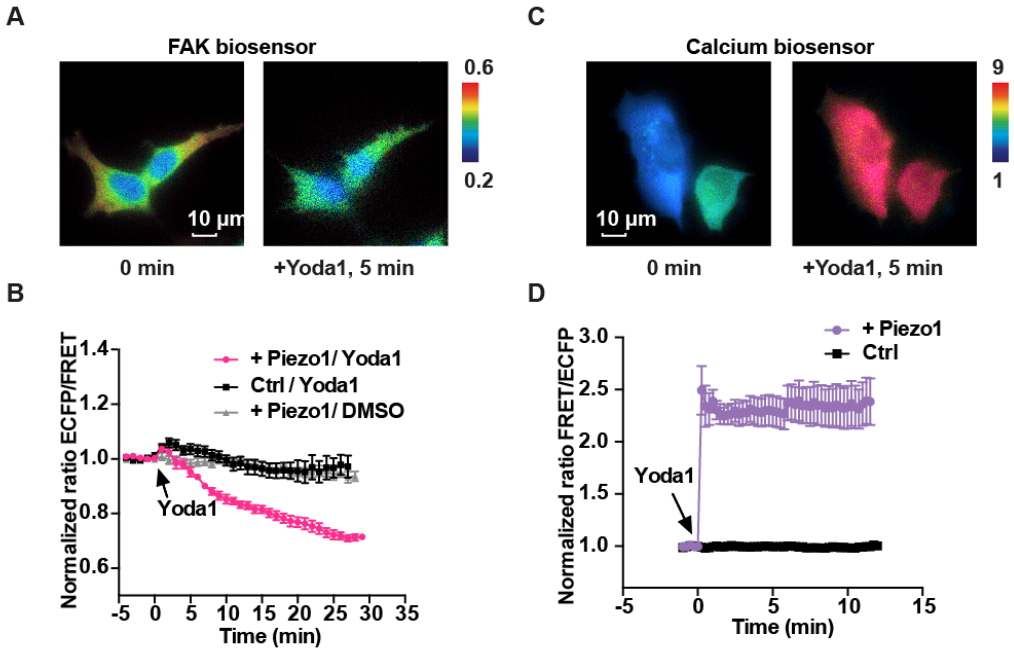

Figure 3.6 The FAK and calcium activation upon Yoda1 stimulation in the Piezo1-expressing HEK cells

(A) The representative ECFP/FRET ratio images of FAK biosensor in Piezo1 expressing HEK cells before and after 25 µM Yoda1 stimulation (Scale bar, 10 µm). (B) The time courses of normalized FRET ratio (Mean ± SEM) of FAK FRET biosensor before and after Yoda1 stimulation with (pink line, n = 10) or without Piezo1 (black line, n = 11). The grey line represents the DMSO control group (n = 8). (C) The representative FRET/ECFP ratio images of the calcium biosensor in the Piezo1-expressing HEK cells before and after 25 µM Yoda1 stimulation (Scale bar, 10 µm). (D) The time courses of normalized FRET ratio (Mean ± SEM) of calcium biosensor in the Piezo1-expressing HEK cells (purple line, n = 9) before and after 25 µM Yoda1 stimulation in culture medium.

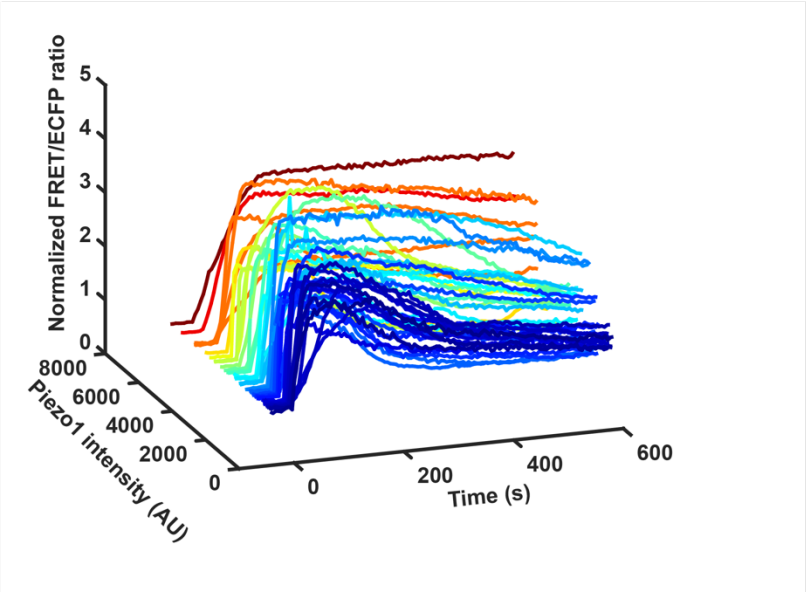

Figure 3.7 Piezo1 level dependent calcium influx upon Yoda1 stimulation in HEK cells.

The time courses of normalized FRET ratio (Mean ± SEM) of d3cpv biosensor before and after 2 μM Yoda1 stimulation in HEK cells expressing different levels of Piezo1 (n = 44).

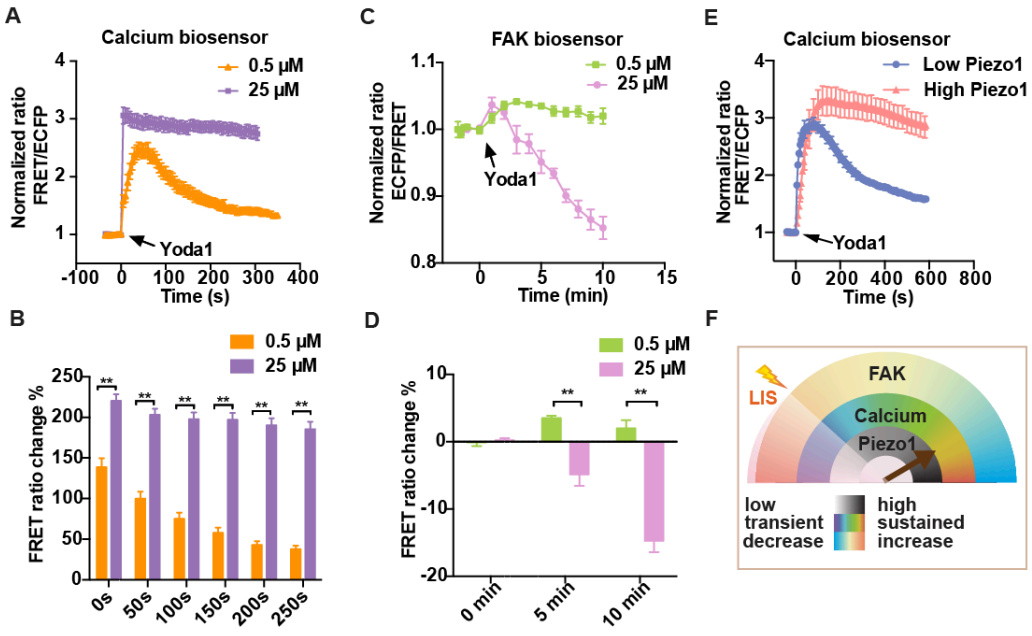

Figure 3.8 The titration of Yoda1 stimulation in the Piezo1-expressing HEK cells.

(**A**) The time courses of normalized FRET ratio of calcium biosensor in the Piezo1-expressing HEK cells upon 0.5 μM (yellow line, n = 10) or 25 μM (purple line, n = 8) Yoda1 stimulation. (**B**) The percentage changes of FRET ratio decrease of calcium biosensor in Piezo1-expressing HEK cells upon 0.5 μM (yellow bar, n = 8) or 25 μM (purple bar, n = 10) Yoda1 stimulation at different time points after they reached the peak. **P* < 0.0001 from student two tailed t-test. (**C**) The time courses of normalized FRET ratio (Mean ± SEM) of FAK FRET biosensor before and after 0.5 μM (green line, n = 8) or 25 μM (pink line, n = 10) Yoda1 stimulation. (**D**) The percentage change of FRET ratio decrease of FAK biosensor in the Piezo1-expressing HEK cells after 0.5 μM (green bar, n = 8) or 25 μM (pink bar, n = 10) Yoda1 stimulation at different time points. **P* < 0.0001. (**E**) The time courses of normalized FRET ratio (Mean ± SEM) of calcium biosensor before and after 2 μM Yoda1 stimulation in cells with high (intensity > 4,650 au., orange line, n = 14) or low (intensity < 1,000 au., Blue line, n = 5) Piezo1 expression. (**F**) A cartoon diagram depicting the activation patterns of Piezo1 on downstream calcium (blue or red represents transient or sustained calcium increase pattern, respectively) and FAK signaling (biphasic: blue or red represents an suppression or activation of FAK activity, respectively) upon stimulation. LIS specifically elicits the lower phase (transient mode) of Piezo1 actions (indicated by the pink shade).

3.7 References

1. Vogel V & Sheetz M (2006) Local force and geometry sensing regulate cell functions. *Nat Rev Mol Cell Biol* 7(4):265-275.

2. Liang X & Boppart SA (2010) Biomechanical properties of in vivo human skin from dynamic optical coherence elastography. *IEEE Trans Biomed Eng* 57(4):953-959.

3. Egan P, Sinko R, LeDuc PR, & Keten S (2015) The role of mechanics in biological and bio-inspired systems. *Nature communications* 6:7418.

4. Park Y, Best CA, Badizadegan K, Dasari RR, Feld MS, Kuriabova T, Henle ML, Levine AJ, & Popescu G (2010) Measurement of red blood cell mechanics during morphological changes. *Proceedings of the National Academy of Sciences of the United States of America* 107(15):6731-6736.

5. Jaalouk DE & Lammerding J (2009) Mechanotransduction gone awry. *Nat Rev Mol Cell Biol* 10(1):63-73.

6. Ranade SS, Syeda R, & Patapoutian A (2015) Mechanically Activated Ion Channels. *Neuron* 87(6):1162-1179.

7. Coste B, Mathur J, Schmidt M, Earley TJ, Ranade S, Petrus MJ, Dubin AE, & Patapoutian A (2010) Piezo1 and Piezo2 are essential components of distinct mechanically activated cation channels. *Science* 330(6000):55-60.

8. Coste B, Xiao B, Santos JS, Syeda R, Grandl J, Spencer KS, Kim SE, Schmidt M, Mathur J, Dubin AE, Montal M, & Patapoutian A (2012) Piezo proteins are pore-forming subunits of mechanically activated channels. *Nature* 483(7388):176-181.

9. Li J, Hou B, Tumova S, Muraki K, Bruns A, Ludlow MJ, Sedo A, Hyman AJ, McKeown L, Young RS, Yuldasheva NY, Majeed Y, Wilson LA, Rode B, Bailey MA, Kim HR, Fu Z, Carter DA, Bilton J, Imrie H, Ajuh P, Dear TN, Cubbon RM, Kearney MT, Prasad KR, Evans PC, Ainscough JF, & Beech DJ (2014) Piezo1 integration of vascular architecture with physiological force. *Nature* 515(7526):279-282.

10. Cahalan SM, Lukacs V, Ranade SS, Chien S, Bandell M, & Patapoutian A (2015) Piezo1 links mechanical forces to red blood cell volume. *eLife* 4.

11. Li C, Rezania S, Kammerer S, Sokolowski A, Devaney T, Gorischek A, Jahn S, Hackl H, Groschner K, Windpassinger C, Malle E, Bauernhofer T, & Schreibmayer W (2015) Piezo1 forms mechanosensitive ion channels in the human MCF-7 breast cancer cell line. *Scientific reports* 5:8364.

12. McHugh BJ, Murdoch A, Haslett C, & Sethi T (2012) Loss of the integrin-activating transmembrane protein Fam38A (Piezo1) promotes a switch to a reduced integrin-dependent mode of cell migration. *PloS one* 7(7):e40346.

13. Lokhandwalla M, McAteer JA, Williams JC, Jr., & Sturtevant B (2001) Mechanical haemolysis in shock wave lithotripsy (SWL): II. In vitro cell lysis due to shear. *Physics in medicine and biology* 46(4):1245-1264.

14. Rau KR, Quinto-Su PA, Hellman AN, & Venugopalan V (2006) Pulsed laser microbeam-induced cell lysis: time-resolved imaging and analysis of hydrodynamic effects. *Biophysical journal* 91(1):317-329.

15. Compton JL, Luo JC, Ma H, Botvinick E, & Venugopalan V (2014) High-throughput optical screening of cellular mechanotransduction. *Nature photonics* 8:710-715.

16. Lu S, Wang Y, Huang H, Pan Y, Chaney EJ, Boppart SA, Ozer H, Strongin AY, & Wang Y (2013) Quantitative FRET imaging to visualize the invasiveness of live breast cancer cells. *PloS one* 8(3):e58569.

17. Mitra SK, Hanson DA, & Schlaepfer DD (2005) Focal adhesion kinase: in command and control of cell motility. *Nat Rev Mol Cell Biol* 6(1):56-68.

18. Palmer AE & Tsien RY (2006) Measuring calcium signaling using genetically targetable fluorescent indicators. *Nature protocols* 1(3):1057-1065.

19. Seong J, Ouyang M, Kim T, Sun J, Wen PC, Lu S, Zhuo Y, Llewellyn NM, Schlaepfer DD, Guan JL, Chien S, & Wang Y (2011) Detection of focal adhesion kinase activation at membrane microdomains by fluorescence resonance energy transfer. *Nature communications* 2:406.

20. Rau KR, Guerra A, Vogel A, & Venugopalan V (2004) Investigation of laser-induced cell lysis using time-resolved imaging. *Appl Phys Lett* 84(15):2940-2942.

21. Gomez-Godinez V, Preece D, Shi L, Khatibzadeh N, Rosales D, Pan Y, Lei L, Wang Y, & Berns MW (2015) Laser-induced shockwave paired with FRET: a method to study cell signaling. *Microscopy research and technique* 78(3):195-199.

22. Syeda R, Xu J, Dubin AE, Coste B, Mathur J, Huynh T, Matzen J, Lao J, Tully DC, Engels IH, Petrassi HM, Schumacher AM, Montal M, Bandell M, & Patapoutian A (2015) Chemical activation of the mechanotransduction channel Piezo1. *eLife* 4.

23. Uhlen M, Fagerberg L, Hallstrom BM, Lindskog C, Oksvold P, Mardinoglu A, Sivertsson A, Kampf C, Sjostedt E, Asplund A, Olsson I, Edlund K, Lundberg E, Navani S, Szigyarto CA, Odeberg J, Djureinovic D, Takanen JO, Hober S, Alm T, Edqvist PH, Berling H, Tegel H, Mulder J, Rockberg J, Nilsson P, Schwenk JM, Hamsten M, von Feilitzen K, Forsberg M, Persson L, Johansson F, Zwahlen M, von Heijne G, Nielsen J, & Ponten F (2015) Proteomics. Tissue-based map of the human proteome. *Science* 347(6220):1260419.

24. Yang XN, Lu YP, Liu JJ, Huang JK, Liu YP, Xiao CX, Jazag A, Ren JL, & Guleng B (2014) Piezo1 is as a novel trefoil factor family 1 binding protein that promotes gastric cancer cell mobility in vitro. *Dig Dis Sci* 59(7):1428-1435.

25. Bagriantsev SN, Gracheva EO, & Gallagher PG (2014) Piezo proteins: regulators of mechanosensation and other cellular processes. *The Journal of biological chemistry* 289(46):31673-31681.

26. Giannone G, Ronde P, Gaire M, Haiech J, & Takeda K (2002) Calcium oscillations trigger focal adhesion disassembly in human U87 astrocytoma cells. *The Journal of biological chemistry* 277(29):26364-26371.

27. Kaczmarek E, Erb L, Koziak K, Jarzyna R, Wink MR, Guckelberger O, Blusztajn JK, Trinkaus-Randall V, Weisman GA, & Robson SC (2005) Modulation of endothelial cell migration by extracellular nucleotides: involvement of focal adhesion kinase and phosphatidylinositol 3-kinase-mediated pathways. *Thromb Haemost* 93(4):735-742.

Chapter 4 The development of remoted controlled mechanogenetics for cancer immunotherapy

4.1 Abstract

While cell-based immunotherapy, especially chimeric antigen receptor (CAR)-expressing T cells, is becoming a paradigm-shifting therapeutic approach for cancer treatment, there is a lack of general methods to remotely and non-invasively regulate genetics in live mammalian cells and animals for cancer immunotherapy within confined local tissue space. To address this limitation, we have identified a mechanically sensitive Piezo1 ion channel (mechanosensor) activatable by ultrasound stimulation and integrated it with engineered genetic circuits (genetic transducer) in live HEK293T cells to convert the ultrasound-activated Piezo1 into transcriptional activities. We have further engineered Jurkat T cell line and primary T cells (periphery blood mononuclear cells, PBMCs) to remotely sense the ultrasound wave and transduce it into transcriptional activation for the CAR expression to recognize and eradicate target tumor cells. This approach is modular and can be extended for remote-controlled activation of different cell types with a high spatiotemporal precision for therapeutic applications.

4.2 Introduction

With the use of central memory T cells capable of suppressing cancer relapse for several years (1), CAR T cell immunotherapy is transforming cancer therapy (2). However, major challenges remain for CAR-based immunotherapy against solid tumors. For instance, the non-specific targeting of the CAR-T cells against normal/non-malignant tissues (on-target but off-tumor toxicities) can be life-threatening (3). There is hence an urgent need for the control of CAR-T cell activation with a high spatiotemporal precision.

Existing methods to control genetic activities typically rely on chemical inducers (e.g. dimerizers), radio waves, and magnetic or light activation (e.g. optogenetics). Chemical inducers, radio waves, and magnetic field typically lack spatial resolution, with radio and magnetic waves mostly requiring the signal amplification and transmission by nanoparticles (or particle aggregates) to stimulate genetically engineered cells (4-7). Although light activation or optogenetics can enable a precise control of genetic regulation in space and time, it cannot reach deep tissues (8). In contrast, ultrasound and its associated energy can be safely and non-invasively delivered into small volumes of tissue deep inside the body with high spatiotemporal resolutions (9, 10). In fact, high frequency ultrasound (HFU) can be focused for mechanical stimulation of single cells at a subcellular region of less than 10 μm (11). Microbubbles, which have been well established as ultrasound imaging contrast agents and approved by the FDA for clinical use (12), can further amplify the impact of low-frequency

ultrasound stimulation with the capability of long-distance penetration on cells physically coupled to microbubbles, as a result of a large difference in acoustic impedance between the surrounding media and the air inside the bubbles (13-15).

We have developed a modular method to engineer cells that can sense ultrasound stimulation applied remotely and non-invasively to control genetics and CAR protein expression for recognizing antigens to kill the target tumor cells. This method utilizes Piezo1 ion channel as a mechanical sensor (Fig. 1*A*), which has been identified as a component of mechanically activated (MA) cation channels (16) and are inherently mechanosensitive (17). The ultrasound-stimulation of Piezo1 and the consequent calcium influx can activate calcium-sensitive phosphatase calcineurin to dephosphorylate a transcription factor, the nuclear factor of activated T-cells (NFAT), which can then translocate to the nucleus for the activation of NFAT response element (RE) to drive the expression of designed target genes (18).

4.3 Materials and Methods

4.3.1 Ultrasonic Transducer and Stimulation System

Ultrasonic transducers were fabricated with standard procedures (19). The center frequency of the ultrasonic transducers is 2 MHz and the aperture size is 5 mm. The transducer is unfocused with the natural focus at approximately 8.3 mm. The 150 MHz high frequency focused transducer has the focus at approximately 1mm. The developed 2 MHz or 150 MHz ultrasonic transducers were integrated with a Nikon FRET microscope to stimulate cells using ultrasound as well as to monitor molecular signals using FRET imaging. The ultrasonic transducer was connected to a 3D

mechanical stage to control the position of the transducer. A pulser/receiver (Olympus, Waltham, MA) and an oscilloscope (Lecroy, Chestnut Ridge, NY) were used to place the natural focus of the ultrasonic transducer at the target cell as shown in Fig. 1*B*. To stimulate HEK293T cells for calcium imaging, the 150 MHz ultrasonic transducer was positioned perpendicular to the dish bottom surface. The transducer was submerged in the medium 1 mm away from the cells. (Fig. S2*A*). The resultant peak-to-peak voltage (V_{pp}) was 22.12 V – 31.6 V. The acoustic pressure is ~ 0.6 MPa for the 2 MHz transducer at the site of the bubbles, and ~ 3 MPa at the focus site for the 150 MHz high-frequency transducer. The duration of 150 MHz ultrasound stimulation was 5 μs – 10 μs. The 2 MHz ultrasonic transducer was positioned at a 45° angle relative to the dish bottom surface to avoid standing wave in a dish. The transducer was submerged in the medium 8.3 mm away from the cells (Fig. S1*A*). The electrical signals were generated by a function generator and a power amplifier to drive the ultrasonic transducer. The resultant peak-to-peak voltage (V_{pp}) was 22.12 V - 31.6 V. For 2 MHz transducer, pulse repetition frequency (PRF) was 5 Hz and the duty factor was 10%. The duration of ultrasound stimulation was 5 sec for calcium imaging, and 10 min for gene induction of cells. During the 10 min ultrasound application, cells on the glass bottom dish were continuously scanned by ultrasound. Therefore, there were multiple calcium transients generated during this time period. In fact, results revealed varying strengths of mechanogenetic effects with different durations of ultrasound stimulation (Fig. S6*B*). The efficiency for microbubbles to be attached to biotinylated surface of suspended cells is high. When the number ratio of microbubble/cell is at 40, there is a significant binding (> 50%). When the number ratio of microbubble/cell is at 400, virtually 100% of the

cells are bound to microbubbles. In our experiments, we maintained the number ratio of microbubble/cell at around 100, and on average, 3-4 microbubbles were attached to each suspended T cell.

A glass tube was used to contain Jurkat cells and PBMCs and the ultrasonic transducer was positioned with a 45° angle with respect to the glass surface for ultrasound stimulation. The transducer was placed at 8.3 mm away from the cell - microbubble mixture inside the glass tube as shown in Fig. S1*B*. For the glass tube experiments, V_{pp} was 22.12 V - 31.6 V. PRF and duty factor were 100 Hz and 1%, respectively. The duration of ultrasound stimulation was 10 min for these suspension cells.

4.3.2 Image Acquisition

The ultrasound stimulation/FRET imaging system was integrated with a Nikon fluorescence microscope for FRET imaging. Images were collected by a Nikon and a cooled charge-coupled device (CCD) camera using MetaFluor 6.2 and MetaMorph software (Universal Imaging, Downing town, PA) with a 420DF40 excitation filter, a 455DCXRU dichroic mirror, and two emission filters controlled by a filter changer (480DF40 for CFP and 535DF35 for YFP). A neutral density filter was used to control the intensity of the excitation light. The fluorescence intensity of non-transfected cells was quantified as the background signals and subtracted from the CFP and YFP signals on transfected cells. The pixel-by-pixel ratio images of YFP/CFP were calculated based on the background-subtracted fluorescence intensity images of CFP and YFP by the Metafluor program to allow quantification and statistical analysis of FRET responses.

The emission ratio images were shown in the intensity modified display (IMD) mode (20).

4.3.3 Constructs and Plasmids

The construct of the mPiezo1-tdTomato was obtained from Dr. Patapoutian's lab (21). The D3cpv calcium FRET biosensor was previously described (22). The nucleotide sequence encoding the CD19-CAR, including the anti-human CD19 scFv, the human CD8α hinge, CD28 transmembrane and co-stimulation domain, the human 4-1BB co-stimulation domain and CD3ζ ITAM signaling domain were synthesized by Integrated DNA Technologies (1). Sequences encoding the VPR were obtained from Addgene (plasmids #63798) (23). The plasmid containing sequences encoding the calcium dependent response elements and minimal promoter was a kind gift from Dr. Jeffrey Friedman's lab at Rockefeller University. Nuclear factor of activated t-cells (NFAT) responding elements (GGAGGAAAAACTGTTTCATACAGAAGGCGT) and minimal promoter (AGAGGGTATATAATGGAAGCTCGAATTCCAG) were from pGL4.30[*luc2P*/NFAT-RE/Hydro] (Promega, Madison, WI). The sequences for SRE is CCATATTAGG and CRE is TGACGTCA. SRE, CRE, NFAT response elements were each used in triplicate. Standard molecular cloning techniques (PCR, restriction digestion, ligation, etc.) were applied to construct CAR expression plasmids and produce lentivirus using a second-generation self-inactivating lentiviral vector pHR'SIN:CSW.

4.3.4 Cell culture and reagents

Human embryonic kidney cells (HEK293T), Jurkat T cells and Toledo cells were purchased from ATCC. HEK293T cells were cultured in Dulbecco's modified eagle medium with 10% FBS (Gibco, Carlsbad, California), 2 mM L-glutamine, 1 unit/ml penicillin, 100 μg/ml streptomycin, and 1mM sodium pyruvate. Jurkat cells and Toledo cells were maintained in RPMI-1640 medium supplemented with 10% FBS, penicillin and streptomycin. Primary human T cells were isolated from anonymous healthy donor's blood after apheresis (San Diego Blood Bank, San Diego, CA). Purified PBMCs were cryopreserved in culture RPMI-1640 medium supplemented with 10% DMSO until use. During experiments, PBMCs were maintained in RPMI-1640 medium supplemented with 10% FBS, and 30 units/ml IL-2 (PeproTech, Rocky Hill, NJ). All cells were cultured at 37 °C with 5% CO_2. Ionomycin were purchased from Sigma.

4.3.5 Cell preparation for ultrasound stimulation

For HEK293T cells, Targestar™-SA lipid microbubbles (Targeson, La Jolla, CA) (1×10^9/mL) were mixed with biotinylated Arg-Gly-Asp (RGD) peptides (0.01 mg/mL) (Peptide International, Louisville, KY) for 20 min (24). Immediately after removing the culture media in the dish, 5 μl of the microbubble-RGD mixture was added into the dish. The dish was then flipped upside down for 5 min to allow microbubbles to float up and attach to the cell membrane.

For Jurkat cells and PBMCs, membrane proteins on the cell surface were biotinylated by EZ-Link™ Sulfo-NHS-Biotin (2 mM) (Thermo Scientific, Rockford,

IL) for 15 min and washed with PBS before the cells were incubated with and coupled to Targestar™ microbubbles.

4.3.6 Gene activation assays

For luciferase-based gene expression assay, the pRL-TK plasmid (Promega, Madison, WI) was co-transfected with the ReCoM luciferase reporters using FUGENE 6 to normalize for transfection efficiency. Luciferase activity was assayed 36 - 48 hours after transfection, using a dual-luciferase reporter assay system (Promega, Madison, WI). In brief, cells were pelleted by centrifugation at 300g for 3 min, re-suspended in lysis buffer for 15 min, and then processed with a plate reader (Tecan infinite M1000 Pro) for luciferase assay and reading quantifications.

For flow cytometry assay of fluorescent reporter expression, cells were re-suspended in FACS wash buffer (PBS + 0.5% BSA) and processed with a BD accuri C6 cytometer. FlowJo software (TreeStar) was used to quantify fluorescence percentages and intensities.

For quantitative-PCR (Q-PCR) assay of CD19-CAR gene expression. Total RNA from cells was extracted by TRIzol. cDNA was synthesized with 500ng of total RNA using M-MLV transcriptase. Quantification of RNA levels was carried out using real-time PCR (KAPA SYBR FAST qPCR kit) (KAPA) and normalized to the level ACTB gene expression. Sequence of PCR primers are as follows: ReCoM-CAR, 5'-AAGTCCAGCTCCAGCAATCC-3'; and 5'-GGAAGGCTGACCCCACTAAC -3'.

4.3.7 Lentiviral Infection of primary T cells

Pantropic VSV-G pseudotyped lentivirus was produced from Lenti-X 293T cells (Clontech Laboratories #632180) co-transfected with a pHR'SIN:CSW transgene expression vector, and the viral packaging plasmids pCMVdR8.91 and pCMV-VSV-G using Lipofectamine 2000 (Life Technologies). Viral medium/supernatant was collected 48 hr after transfection for infection. 3 days prior to viral infection, primary human T cells were thawed and activated using 2 μg/ml PHA (Thermo Scientific, Rockford, IL) in RPMI-1640 medium supplemented with 10% FBS, penicillin and streptomycin for 72 hr. PHA was then removed before cells were infected. Infected primary T cells (PBMCs) were maintained at ~10^6 /mL in culture RPMI medium supplemented with 30 units/ml IL2 for 5 days before experiments were conducted.

4.3.8 Verifying CAR expression on T cells:

Jurkat or primary human T cells were re-suspended in FACS wash buffer (PBS + 0.5% BSA) and stained with Alexa Fluor® 647 AffiniPure $F(ab')_2$ Fragment Goat Anti-Mouse IgG antibody (JacksonImmunoResearch, West Grove, PA). Stained cells were washed three times in washing buffer PBS + 0.5% BSA, and processed with a BD accuri C6 cytometer. FlowJo software (TreeStar) was used to quantify Alexa dye and/or mCherry fluorescence intensities and percentages.

4.3.9 Quantitation of CD69 surface expression

Jurkat T cells after ultrasound activation were mixed with target Toledo cells at a 1:1 T/target cell ratio in a 24-well plate. After 24 hr incubation, cells were pelleted by

centrifugation at 300 g for 5 min. Cells were re-suspended in FACS wash buffer (PBS + 0.5% BSA) and stained with APC anti-human CD69 antibody (BioLegend #310910). Stained cells were washed three times in FACS wash buffer, and processed with a BD accuri C6 cytometer. FlowJo software (TreeStar) was applied to compare Alexa fluorescence intensities of gated T cells (unique forward/side scatters) in samples. Data plots were generated using Prism software (GraphPad).

4.3.10 Luciferase based cell killing assay

PBMCs after ultrasound activation were mixed with NALM-6 target cells at a 10:1 T/target cell ratio in a 96-well plate. After 24 hr incubation, cells were pelleted by centrifugation at 300 g for 5 min. Cells were re-suspended in 50 µl lysis buffer (Promega) and processed with a plate reader (Tecan infinite M1000 Pro) for luciferase assay.

4.4 Results

We first examined whether the ultrasound-induced mechanical stimulation can activate the Piezo1 channel to elicit calcium influx. HEK293T cells co-transfected with Piezo1-tdTomato and D3cpv FRET calcium biosensor were examined by an ultrasound-FRET imaging system (Figure. 4.1B and Figure 4.2) (25). Upon a focused HFU (150 MHz) stimulation with a distance of 1 mm, a Piezo1-dependent calcium influx was clearly detected in the target cell (Figure 4.2), suggesting that Piezo1 can serve as a mechano-sensor to sense the ultrasound stimulation. For this 150 MHz focused

transducer, the focused acoustic pressure applied on the cell membrane can directly activate the Piezo1 ion channel to mediate calcium influx. However, this high-frequency 150 MHz transducer has limited working distance (1 mm) that is much shorter than the effective working distance of centimeters with low-frequency transducers. To develop a technology for the remote control of gene activities in live cells, we reasoned that microbubbles mechanically coupled to Piezo1 can be applied to amplify the mechanical waves of low-frequency 2 MHz ultrasound at a distance in centimeters (4-8). Indeed, microbubbles with a 2-μm diameter can be stimulated at a depth of 5 cm by a low-frequency ultrasound transducer. Hence, microbubbles were coated with streptavidin and coupled to biotinylated RGD peptides, which were engaged with the membrane receptor integrins and connected to Piezo1 via cytoskeleton and membrane tension . Upon 2-MHz ultrasound stimulation at a distance of ~ 1 cm, calcium influx into the cells was immediately detected in the presence of calcium-containing HBSS media (Figure 4.1C), but not in HBSS media without calcium. In control HEK293T cells transfected only with a calcium biosensor but without Piezo1, there was no significant calcium influx in HBSS media with or without calcium. This 2-MHz transducer activates Piezo1 channel differently from that of 150-MHz. For 2-MHz transducer, it depends on several factors, e.g. the oscillation of microbubbles and possibly the resulting fluid microstreaming/shear stress associated with the ultrasound excitation. Indeed, the piezo1-expressing cells without microbubble coupling did not respond to ultrasound to trigger calcium signals. Ultrasound power was robustly controlled in a range between 22.1 V and 31.6 V in order to create a sufficient ultrasound wave to

mechanically stimulate the cells, without causing damage of the target cells (Figure 4.3). Indeed, intermittent ultrasound waves could be applied to elicit multiple calcium waves (Figure 4.3), suggesting minimal ultrasound-induced alteration of the target cells.

We then examined whether the ultrasound-induced calcium influx can be applied to control gene expression. Genetic transducing modules (GTMs) were engineered to transmit the calcium-mediated NFAT activation and other related signaling into genetic activities. A one-stage GTM design was developed consisting of three calcium responding elements *in cis*: serum responding element (SRE), cyclic adenosine monophosphate response element (CRE), and NFAT response element (NFAT RE), placed in tandem upstream of the minimal promoters controlling target gene expression (5) (Figure 4.4A_a-b). In order to reduce the potentially leaky protein expression in cells and enhance the induction specificity upon stimulation, a two-stage GTM was designed using a potent tripartite transcriptional activator VPR (23) (Figure 4.4A_c-f). In these designs, the first induced product upon ultrasound stimulation and calcium influx is a DNA binding domain (DBD) LexA fused to VPR (LexA-VPR). This LexA-VPR upon induction activates a second gene response element (LexA RE) for the expression of target genes (Figure 4.4A_c-f). Two minimal promoters were compared in their efficiency and specificity; the one derived from the CMV promoter was more robust but exhibited a higher basal level noise than the other one derived from a commercial vector pGL4.30 (Promega). Collectively, six potential candidates were designed (Figure 4.4A), with luciferase or fluorescent proteins as target reporter genes to characterize the activation potency. Indeed, 2-MHz ultrasound stimulation for 10 min

(see detailed information in Materials and Methods) caused a clear induction of reporter genes measured by luciferase activities (Figure 4.4B), similar to the chemical induction by ionomycin (Figure 4.4C). We observed a significant difference in the basal and induced expression levels of target genes upon stimulation with these six different designs (Figure 4.4A and B). Among them, design a was chosen as the candidate for further applications due to its simplicity, low basal level and more efficient activation potency. Indeed, the inducible promoter based on design a can be activated by ultrasound stimulation to clearly drive the expression of a GFP variant mNeonGreen (Figure 4.4D). These results indicate that the mechanosensor Piezo1 and GTMs can be engineered and integrated to coordinate with the endogenous molecular network for the sensing of remote ultrasound stimulation to guide gene activations. We also showed that RGD-tagged microbubbles' engagement of integrins on the cell surface alone was not sufficient to significantly activate the specifically designed gene expression controlled by genetic transducers (Figure 4.5A), suggesting a high specificity of the ultrasound controllable gene activation in our system. While the 10-min application can induce relatively robust mechanogenetic effects, shorter durations of ultrasound stimulation can also induce gene expression, but with a weaker efficiency (Figure 4.5B).

We then applied this system of remote-control mechanogenetics (ReCoM) based on design a to control the expression of anti-CD19 CAR in Jurkat T cell lines and primary human T cells (peripheral blood mononuclear cells, PBMCs) for cancer immunotherapy since anti-CD19 CAR and CD19 have been well established as an interaction pair for the immunotherapy of hematopoietic malignancies (2, 26). Jurkat

and PBMC T cells express high levels of endogenous Piezo1 (27). Indeed, when microbubbles coated by streptavidin were coupled to the biotinylated surface membrane of Jurkat cells without the introduction of additional exogenous Piezo1 (Figure 4.6A), calcium influx was observed upon ultrasound stimulation (Figure 4.6B). Further experiments validated ReCoM in controlling the production of mNeonGreen reporter driven by different minimal promoters upon ultrasound stimulation in Jurkat T cells without the need of co-expression of exogenous Piezo1 (Figure 4.7). We then applied ReCoM to control anti-CD19 CAR production by ultrasound in Jurkat cells. The encoding mRNA and expression percentage of anti-CD19 CAR in Jurkat cells was significantly increased after ultrasound stimulation (Figure 4.6D, Figure 4.7C). The Jurkat cells with the ultrasound-induced CAR expression were then incubated with CD19 antigen-expressing target tumor cells (Toledo lymphoma tumor cells which express high levels of CD19) (28). Upon the engagement of ultrasound-induced Jurkat and target Toledo cells for 24 hr, the surface marker CD69 reflecting T cell activation (29) was clearly upregulated in the Jurkat cells (Figure 4.7E and F). These results indicate that the ultrasound-induced CAR production in Jurkat T cells can functionally mediate the engagement with antigens on the target tumor cells and activate Jurkat cells.

We then applied ReCoM to remotely control the CAR production in PBMCs and examine their efficacy in tumor cell killing (Figure 4.8A). Calcium influx in PBMCs can be clearly observed upon ultrasound stimulation (Figure 4.8B). We further measured the ReCoM-mediated expression of anti-CD19 CAR in PBMCs. The average expression level of anti-CD19 CAR was significantly increased after ultrasound

stimulation (Figure 4.8C). These ultrasound-induced PBMCs were incubated with target B cell leukemia cell line (Nalm6) expressing CD19-antigen and luciferase (30, 31), which allowed a convenient tracking of the target tumor cell growth by measuring the luciferase activities. The results of luciferase activity in reflecting Nalm6 cell numbers revealed that the ultrasound-induced ReCoM PBMCs can cause significantly more toxicity of the target Nalm6 cells than the ReCoM PBMCs not exposed to ultrasound or the plain PBMCs exposed to ultrasound but without ReCoM GTMs (Figure 4.8D).

4.5 Discussions

We reported here the development of ReCoM technology to allow the remote and non-invasive control of gene expression in live cells with high spatiotemporal precision using ultrasound. Although there have been disparate trial-and-error approaches to apply ultrasound to mechanically perturb cells and *c. elegans* (32-34), there was no established method as the ReCoM presented here to convert the ultrasound mechanical signals into genetic controls of cells. Indeed, we have demonstrated that this ReCoM system can remotely control the expression of luciferase or GFP in various adherent or suspension cells. We further established that ReCoM is effective in controlling CAR expression in T cells to guide the recognition and eradication of tumor cells for controllable cancer immunotherapy. This system is highly modular as shown by multiple designs of genetic circuits with various basal levels and activation potency, thus allowing continuous evolution and optimization to target multiple types of cancers and precancerous conditions. In summary, ReCoM will usher in a new era in life science

and medical technology by bringing the full power of remote control of gene and cell activation to the scientific and clinical communities for the precise control of therapeutics in space and time.

4.6 Acknowledgements

Chapter 4 is nearly identical to a peer-reviewed article entitled "Mechanogenetics for the remote and noninvasive control of cancer immunotherapy" by Pan Y., Yoon S., Sun J., Huang Z., Lee C., Allen M., Wu Y., Chang YJ., Sadelain M., Shung K.K., Chien S., Wang Y.. This article was published in Proc Natl Acad Sci U S A. 2018 Jan 30;115(5):992-997. The dissertation author was the primary investigator and author of this paper. The authors thank professor Ardem Patapoutian at Scripps Research Institute for the Piezo1 construct. These authors acknowledge the funding source NIH HL121365, GM125379 (S.C. and Y. Wang), CA204704 and CA209629 (Y. Wang), NSF CBET1360341, DMS1361421 (Y. Wang and S.L.), and the Beckman Laser Institute Foundation.

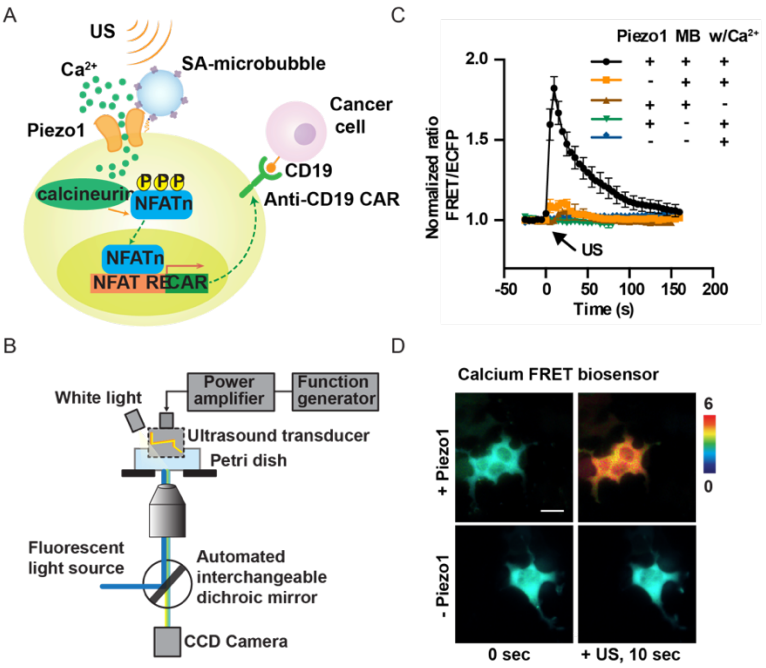

Figure 4.1 Design of synthetic genetic circuits remotely activatable by ultrasound

(A) Schematic drawing of ultrasound-induced cell activation and gene expression. Microbubbles can be coupled to the surface of a cell, where mechanosensitive Piezo1 channels are expressed. Upon exposure to ultrasound waves, the mechanical stimulation can activate the Piezo1 ion channels. The subsequent calcium entry triggers the downstream pathways, including calcineurin activation, NFAT dephoshorylation and translocation into the nucleus. The nucleus-translocated NFAT can bind to upstream response elements to initiate gene expression through one-stage or two-stage genetic transducing modules. (B) Diagram of an integrated system of ultrasound stimulation and FRET imaging. The CCD camera captures fluorescent images of FRET biosensors with two emission filters controlled by a filter changer (480DF40 for CFP and 535DF35 for YFP). The ultrasonic transducer was driven by a function generator and a power amplifier. (C) The time courses of normalized FRET/ECFP ratio (mean ± S.E.M.) of a D3cpv calcium biosensor in HEK293T cells before and after 5 sec ultrasound stimulation under different conditions with or without the presence of the three components (Piezo1, microbubbles, and Ca^{2+}) in the medium: with all three components (black, n = 32), without Piezo1 (yellow, n = 37), without microbubbles (green, n = 10), without Ca^{2+} (brown, n = 14), or without both Piezo1 and microbubbles (blue, n = 11). (D) Representative FRET/ECFP ratio images of D3cpv calcium biosensor in HEK293T cells expressed with (top panels) or without (bottom panels) Piezo1 before (left) and after (right) ultrasound stimulation. Scale bar represents 20 μm.

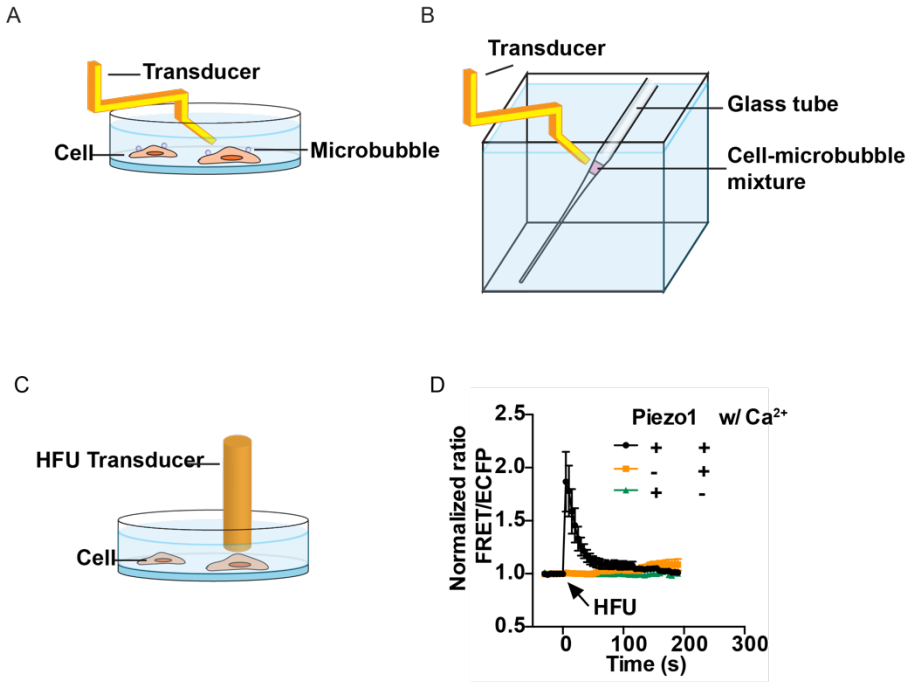

Figure 4.2 The ultrasound stimulation system for cells.

(A) A schematic drawing of ultrasound stimulation on adherent HEK293T cells in a dish. The ultrasonic transducer was positioned at a 45° angle relative to the dish surface, and submerged in the medium 8.3 mm away from the cells on the dish bottom. (B) A schematic drawing of ultrasound stimulation on suspension Jurkat and PBMCs. The cell and microbubble mixture was injected into a glass tube, and ultrasonic transducer was positioned 8.3 mm away from the glass tube surface where cell mixture is located. (C) A schematic drawing of HFU stimulation on HEK293T cells in a dish. The ultrasonic transducer was positioned perpendicular to the dish surface, and submerged in the medium 1 mm away from the cells on the dish bottom. (D) The time courses of normalized FRET/ECFP ratio (mean ± S.E.M.) of a D3cpv calcium biosensor in HEK293T cells before and after HFU stimulation under different conditions with or without the presence of Piezo1 or Ca^{2+} in the medium: with all 2 components (black line, n = 11), without Piezo1 (yellow line, n = 9), without Ca^{2+} (green line, n = 6).

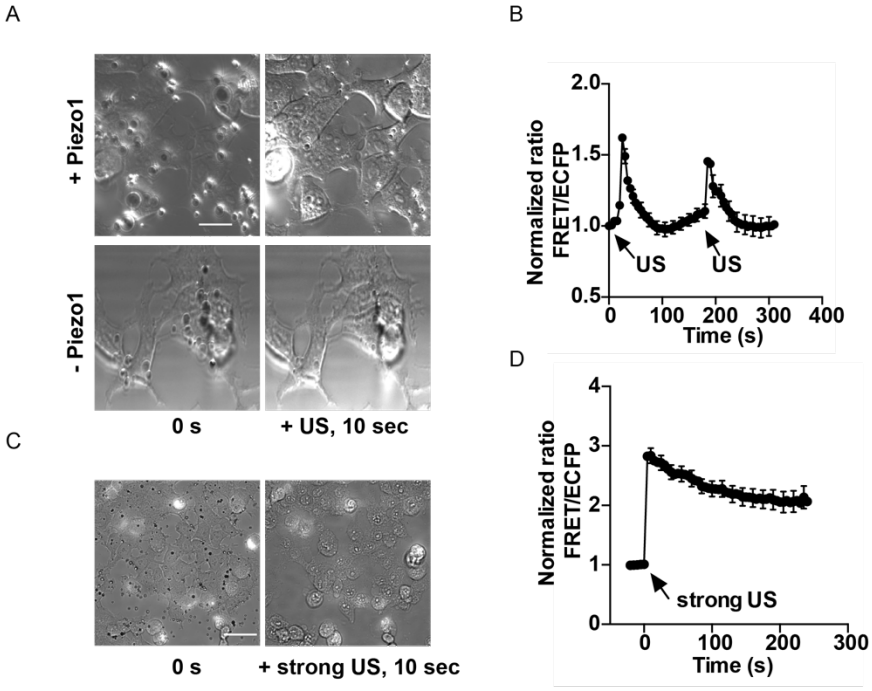

Figure 4.3 The calibration of ultrasound power to avoid cell damage.

(A) The representative phase images of Piezo1 expressing HEK293T cells before (top left) and after (top right) ultrasound stimulation. Cells were alive and not damaged upon stimulation. (B) The time course of normalized FRET ratio (mean ± S.E.M.) of D3cpv calcium biosensor in Piezo1-expressing HEK293T cells (n = 6) before and after multiple ultrasound stimulations. (C) The representative DIC images of HEK293T cells before (top left) and after (top right) strong ultrasound (38 V) stimulation. Cells were damaged upon stimulation. (D) The time course of normalized FRET/ECFP ratio (mean ± S.E.M.) of D3cpv calcium biosensor in Piezo1-expressing HEK293T cells (n = 6) before and after strong and cell-damaging ultrasound stimulation. It is of note that the calcium level was sustained upon damaging stimulation.

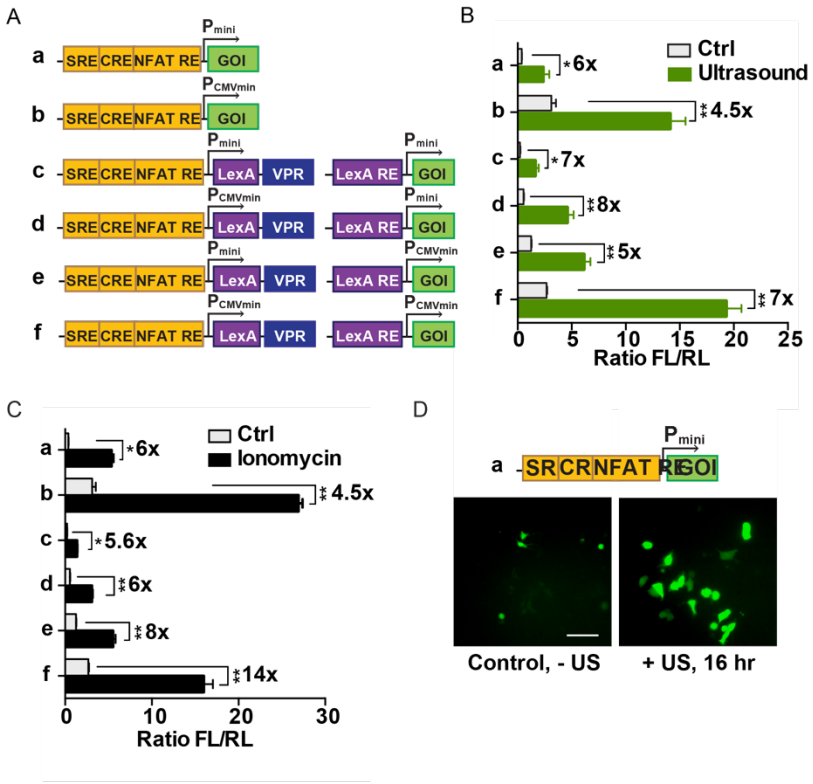

Figure 4.4 Characterization of genetic transducing modules (GTMs) remotely activatable by ultrasound

(A) The design of ReCoM genetic transducing modules (GTMs). Calcium responding elements consisting of SRE, CRE and NFAT RE were followed by target genes of interest (GOI) controlled by minimal promoter (a, P_{min}) or minimal CMV promoter (b, P_{CMVmin}). For two-stage constructs, LexA-VPR was designed as the product of stage 1 gene cassette, which can bind to the LexA responding element and activate stage 2 target genes (c, d, e, f). (B) Ultrasound stimulation induced gene products of different GTMs. Microbubbles-coupled HEK293T cells transfected with Piezo1 and GTMs showed a significant increase in luciferase gene expression upon ultrasound stimulation (n = 3). (C) Ionomycin stimulation induces gene expression. HEK293T cells transfected with Piezo1 and genetic cassettes showed a significant increase in luciferase gene expression 16 hr after ionomycin stimulation (n = 3). (D) Fluorescence microscopy images of HEK293T cells transfected with Piezo1 and gene activation cassette a (mNeonGreen as the reporter) without (left) and 16 hr after (right) ultrasound stimulation (for 10 min). Scale bar represents 40 μm. Error bars indicate S.E.M., *P<0.05, **P<0.01 from two-tailed Student t-test.

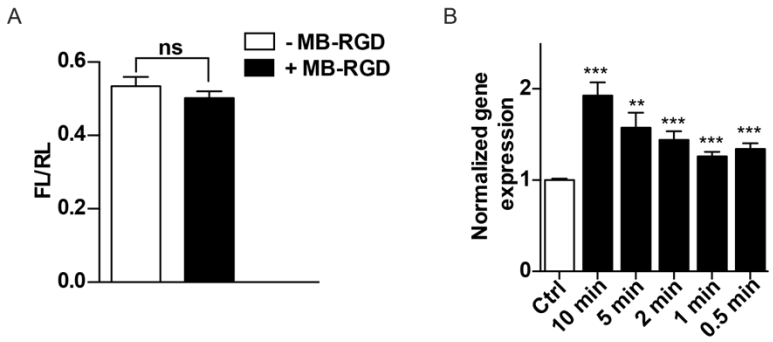

Figure 4.5 The calibration of ultrasound effect on ReCoM responses in HEK293T cells.

(A) Gene activation of ReCoM (design a) before and after RGD-microbubble engagement of the cells. No significant increase in luciferase gene expression was observed upon RGD-microbubble engagement (n = 3). (B) The increased gene expression in HEK293T cells transfected with Piezo1 and genetic transducer design A upon ultrasound stimulation for different durations (n = 3). Error bars indicate S.E.M, ***P < 0.001, **P < 0.01 from two-tailed Student t-test.

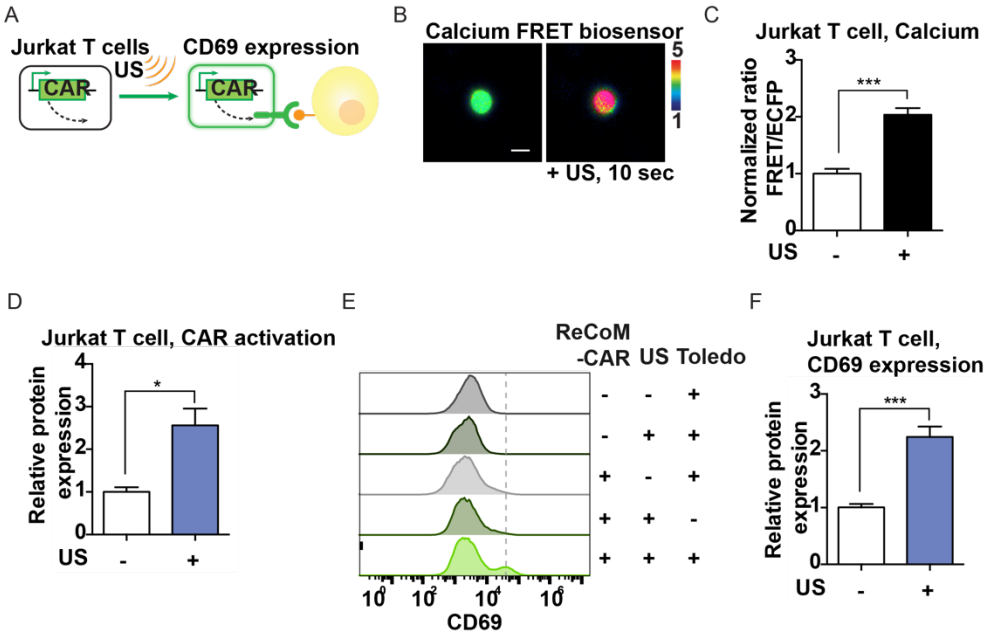

Figure 4.6 Remote-controlled activation of Jurkat T cells with ReCoM

(A) Jurkat cells were transfected with inducible ReCoM-CAR. After ultrasound stimulation, they were mixed with antigen CD19-expressing target tumor cells and evaluated for their activation level (CD69 expression). (B) The representative FRET/ECFP ratio images of D3cpv calcium biosensor in Jurkat cells before (left) and after (right) ultrasound stimulation. Scale bar represents 10 μm. (C) The FRET/ECFP ratio percentage change of D3cpv calcium FRET biosensor averaged among multiple Jurkat cells before and 10 sec after ultrasound stimulation (n = 15). (D) Normalized expression of anti-CD19-CAR in Jurkat cells 16 hr after ultrasound stimulation (n = 3). (E) Representative histograms of T cell activation in Jurkat cells by quantifying the expression of cell surface protein marker CD69. Jurkat and Toledo mixtures were stained with Alexa647-conjugated anti-CD69 antibody and analyzed by flow cytometry. (F) The bar graphs represent CD69 up-regulation (normalized percentage of CD69 positive cells) in ultrasound-induced Jurkat cells upon Toledo cell engagement (n = 8). Error bars indicate S.E.M., *$p < 0.05$, ***$p < 0.001$ from two-tailed Student t-test.

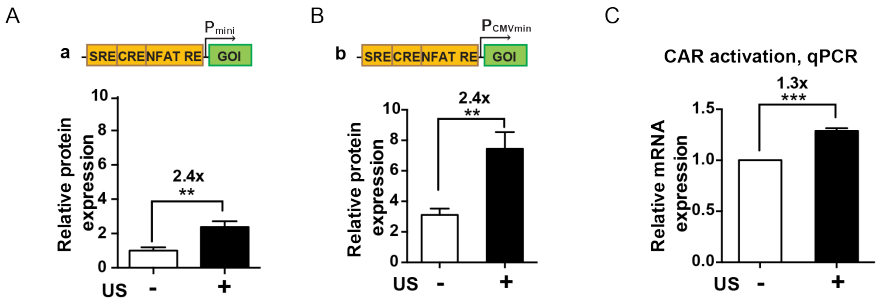

Figure 4.7 The calibration of the ultrasound effect on ReCoM-a (design a) and b (design b) in Jurkat cells.

(A) The increased gene expression in Jurkat cells transfected with ReCoM-a (a minimal promoter derived from the vector pGL4.30 driving mNeonGreen as reporter) upon 10 min ultrasound stimulation (n = 9). (B) The increased gene expression in Jurkat cells transfected with ReCoM-b (a minimal promoter derived from CMV driving mNeonGreen as reporter) upon 10 min ultrasound stimulation (n = 5). (C) Quantitative PCR analysis for the production of mRNA encoding anti-CD19 CAR in Jurkat cells upon 10 min ultrasound stimulation (n = 3). Error bars indicate S.E.M, **P < 0.01 from two-tailed Student t-test.

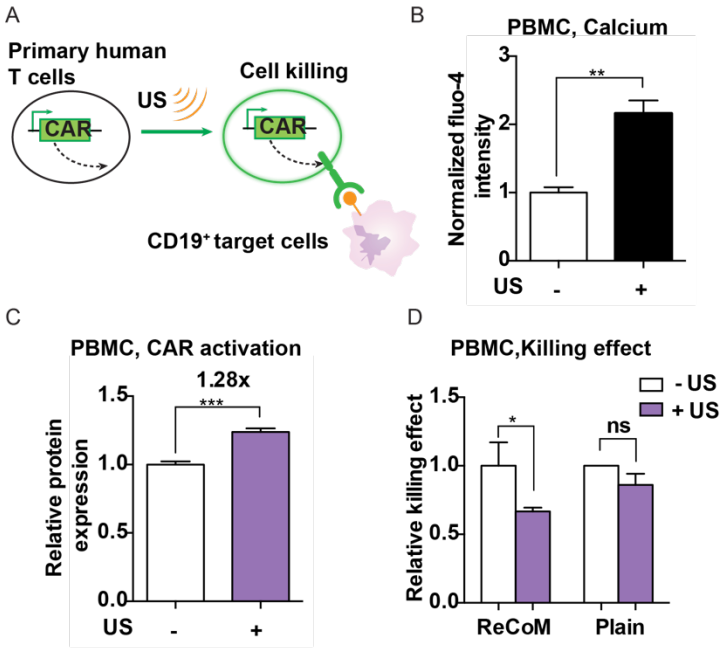

Figure 4.8 Remote-controlled activation of PBMCs with ReCoM.

(A) PBMCs were transfected with inducible ReCoM-CAR. After ultrasound stimulation, they were mixed with antigen CD19-expressing target tumor cells and evaluated for killing efficiency by functional assays. (B) The Fluo-4 calcium indicator intensity change in PBMCs before and after 5 sec ultrasound stimulation (n = 4). (C) Expression of ReCoM-CAR in PBMCs 16 hr after ultrasound stimulation (n = 5). (D) Cytotoxicity of target Nalm6 tumor cells caused by CAR expression upon ultrasound stimulation in PBMCs cells transfected with ReCoM-CAR GTMs, measured by luciferase-based killing assay (n = 4). Cytotoxicity of plain PBMCs upon ultrasound stimulation was also measured (n = 3). Error bars indicate S.E.M., *$p < 0.05$, **$P < 0.01$ from two-tailed Student t-test.

4.7 References

1. Grupp SA, Kalos M, Barrett D, Aplenc R, Porter DL, Rheingold SR, Teachey DT, Chew A, Hauck B, Wright JF, Milone MC, Levine BL, & June CH (2013) Chimeric antigen receptor-modified T cells for acute lymphoid leukemia. *N Engl J Med* 368(16):1509-1518.

2. Fesnak AD, June CH, & Levine BL (2016) Engineered T cells: the promise and challenges of cancer immunotherapy. *Nat Rev Cancer* 16(9):566-581.

3. Morgan RA, Yang JC, Kitano M, Dudley ME, Laurencot CM, & Rosenberg SA (2010) Case report of a serious adverse event following the administration of T cells transduced with a chimeric antigen receptor recognizing ERBB2. *Mol Ther* 18(4):843-851.

4. Seo D, Southard KM, Kim JW, Lee HJ, Farlow J, Lee JU, Litt DB, Haas T, Alivisatos AP, Cheon J, Gartner ZJ, & Jun YW (2016) A Mechanogenetic Toolkit for Interrogating Cell Signaling in Space and Time. *Cell* 165(6):1507-1518.

5. Stanley SA, Gagner JE, Damanpour S, Yoshida M, Dordick JS, & Friedman JM (2012) Radio-wave heating of iron oxide nanoparticles can regulate plasma glucose in mice. *Science* 336(6081):604-608.

6. Stanley SA, Kelly L, Latcha KN, Schmidt SF, Yu X, Nectow AR, Sauer J, Dyke JP, Dordick JS, & Friedman JM (2016) Bidirectional electromagnetic control of the hypothalamus regulates feeding and metabolism. *Nature* 531(7596):647-650.

7. Stanley SA, Sauer J, Kane RS, Dordick JS, & Friedman JM (2015) Remote regulation of glucose homeostasis in mice using genetically encoded nanoparticles. *Nature medicine* 21(1):92-98.

8. Wang X, Chen X, & Yang Y (2012) Spatiotemporal control of gene expression by a light-switchable transgene system. *Nat Methods* 9(3):266-269.

9. Ibsen S, Schutt CE, & Esener S (2013) Microbubble-mediated ultrasound therapy: a review of its potential in cancer treatment. *Drug Des Devel Ther* 7:375-388.

10. Yoon S, Aglyamov S, Karpiouk A, & Emelianov S (2013) The mechanical properties of ex vivo bovine and porcine crystalline lenses: age-related changes and location-dependent variations. *Ultrasound Med Biol* 39(6):1120-1127.

11. Yoon S, Kim MG, Chiu CT, Hwang JY, Kim HH, Wang Y, & Shung KK (2016) Direct and sustained intracellular delivery of exogenous molecules using acoustic-transfection with high frequency ultrasound. *Sci Rep* 6:20477.

12. Lindner JR (2004) Microbubbles in medical imaging: current applications and future directions. *Nat Rev Drug Discov* 3(6):527-532.

13. Chen D, Sun Y, Gudur MS, Hsiao YS, Wu Z, Fu J, & Deng CX (2015) Two-bubble acoustic tweezing cytometry for biomechanical probing and stimulation of cells. *Biophys J* 108(1):32-42.

14. Yoon S, Aglyamov SR, Karpiouk AB, Kim S, & Emelianov SY (2011) Estimation of mechanical properties of a viscoelastic medium using a laser-induced microbubble interrogated by an acoustic radiation force. *J Acoust Soc Am* 130(4):2241-2248.

15. Fan Z, Sun Y, Di C, Tay D, Chen W, Deng CX, & Fu J (2013) Acoustic tweezing cytometry for live-cell subcellular modulation of intracellular cytoskeleton contractility. *Sci Rep* 3:2176.

16. Coste B, Mathur J, Schmidt M, Earley TJ, Ranade S, Petrus MJ, Dubin AE, & Patapoutian A (2010) Piezo1 and Piezo2 are essential components of distinct mechanically activated cation channels. *Science* 330(6000):55-60.

17. Syeda R, Florendo MN, Cox CD, Kefauver JM, Santos JS, Martinac B, & Patapoutian A (2016) Piezo1 Channels Are Inherently Mechanosensitive. *Cell Rep* 17(7):1739-1746.

18. Hogan PG (2017) Calcium-NFAT transcriptional signalling in T cell activation and T cell exhaustion. *Cell Calcium*.

19. Yoon S, Kim MG, Williams JA, Yoon C, Kang BJ, Cabrera-Munoz N, Shung KK, & Kim HH (2015) Dual-element needle transducer for intravascular ultrasound imaging. *J Med Imaging (Bellingham)* 2(2):027001.

20. Wang Y, Botvinick EL, Zhao Y, Berns MW, Usami S, Tsien RY, & Chien S (2005) Visualizing the mechanical activation of Src. *Nature* 434(7036):1040-1045.

21. Cahalan SM, Lukacs V, Ranade SS, Chien S, Bandell M, & Patapoutian A (2015) Piezo1 links mechanical forces to red blood cell volume. *eLife* 4.

22. Palmer AE & Tsien RY (2006) Measuring calcium signaling using genetically targetable fluorescent indicators. *Nature protocols* 1(3):1057-1065.

23. Chavez A, Scheiman J, Vora S, Pruitt BW, Tuttle M, E PRI, Lin S, Kiani S, Guzman CD, Wiegand DJ, Ter-Ovanesyan D, Braff JL, Davidsohn N, Housden BE, Perrimon N, Weiss R, Aach J, Collins JJ, & Church GM (2015) Highly efficient Cas9-mediated transcriptional programming. *Nat Methods* 12(4):326-328.

24. Heureaux J, Chen D, Murray VL, Deng CX, & Liu AP (2014) Activation of a bacterial mechanosensitive channel in mammalian cells by cytoskeletal stress. *Cell Mol Bioeng* 7(3):307-319.

25. Kim TJ, Joo C, Seong J, Vafabakhsh R, Botvinick EL, Berns MW, Palmer AE, Wang N, Ha T, Jakobsson E, Sun J, & Wang Y (2015) Distinct mechanisms regulating mechanical force-induced Ca(2)(+) signals at the plasma membrane and the ER in human MSCs. *eLife* 4:e04876.

26. Maus MV, Grupp SA, Porter DL, & June CH (2014) Antibody-modified T cells: CARs take the front seat for hematologic malignancies. *Blood* 123(17):2625-2635.

27. Petryszak R, Keays M, Tang YA, Fonseca NA, Barrera E, Burdett T, Fullgrabe A, Fuentes AM, Jupp S, Koskinen S, Mannion O, Huerta L, Megy K, Snow C, Williams E, Barzine M, Hastings E, Weisser H, Wright J, Jaiswal P, Huber W, Choudhary J, Parkinson HE, & Brazma A (2016) Expression Atlas update--an integrated database of gene and protein expression in humans, animals and plants. *Nucleic Acids Res* 44(D1):D746-752.

28. Kochenderfer JN, Feldman SA, Zhao Y, Xu H, Black MA, Morgan RA, Wilson WH, & Rosenberg SA (2009) Construction and preclinical evaluation of an anti-CD19 chimeric antigen receptor. *J Immunother* 32(7):689-702.

29. Simms PE & Ellis TM (1996) Utility of flow cytometric detection of CD69 expression as a rapid method for determining poly- and oligoclonal lymphocyte activation. *Clin Diagn Lab Immunol* 3(3):301-304.

30. Brentjens RJ, Santos E, Nikhamin Y, Yeh R, Matsushita M, La Perle K, Quintas-Cardama A, Larson SM, & Sadelain M (2007) Genetically targeted T cells eradicate systemic acute lymphoblastic leukemia xenografts. *Clin Cancer Res* 13(18 Pt 1):5426-5435.

31. Zhao Z, Condomines M, van der Stegen SJ, Perna F, Kloss CC, Gunset G, Plotkin J, & Sadelain M (2015) Structural Design of Engineered Costimulation Determines Tumor Rejection Kinetics and Persistence of CAR T Cells. *Cancer Cell* 28(4):415-428.

32. Legon W, Sato TF, Opitz A, Mueller J, Barbour A, Williams A, & Tyler WJ (2014) Transcranial focused ultrasound modulates the activity of primary somatosensory cortex in humans. *Nature neuroscience* 17(2):322-329.

33. Tufail Y, Matyushov A, Baldwin N, Tauchmann ML, Georges J, Yoshihiro A, Tillery SI, & Tyler WJ (2010) Transcranial pulsed ultrasound stimulates intact brain circuits. *Neuron* 66(5):681-694.

34. Ibsen S, Tong A, Schutt C, Esener S, & Chalasani SH (2015) Sonogenetics is a non-invasive approach to activating neurons in Caenorhabditis elegans. *Nat Commun* 6:8264.

Chapter 5 Conclusion

5.1 Conclusion

Fluorescent proteins (FPs) and their derived biosensors, such as those based on fluorescence resonance energy transfer (FRET), have allowed the visualization of dynamic molecular activities at subcellular levels in live cells (1). Optogenetics integrating optical and genetic methods has enabled the control of specific molecular events in living systems with high spatiotemporal resolutions (2-5). The ultrasound-controllable mechanogenetics can non-invasively manipulate cells deep in the body for the control of physiological and therapeutic outcomes, hence bringing the full power of remote control of gene and cell activation to the general scientific and clinical community, similar to how fluorescent proteins and optogenetics have revolutionized live biological sensing and actuating. This dissertation sought to develop a suite of tools towards the non-invasive sensing and manipulation of molecular activities in live cells.

First, a FRET based EphA4 molecular biosensor was developed. The development of the biosensor enables visualization of EphA4 activity in single live cells with high spatial and temporal resolution. The results suggest that not only did we develop a potent tool for sensing molecular activities live time, but also indicated potentials in point-of-care cancer diagnostic tool. On the other hand, we sought to develop a laser based mechanical stimulation tools and molecular biosensors to activate and study engineered cells. Together, Chapter 1 and Chapter 2 built the basis for

developing and integrating engineered molecular tools with novel clinical therapeutic devices.

Second, a shift in the dissertation to engineer a remote controlled mechanogenetics system, leads to the coupling of mechanical stimulations and molecular tools for controlled therapeutics. This mechanogenetic system integrates ultrasound mediated mechanical stimulation and gene activation of CD19CAR for application in cancer immunotherapy. Future directions include removing the requirement of microbubbles in the system for more controllable and safer *in vivo* applications; optimizing molecular transducing modules for better contrast before and after ultrasound stimulation.

By combining the orthogonal mechanogenetic and optogenetic controls, fully controllable live cells can be developed, activated or deactivated at any given time for cellular studies and therapeutic approaches. In addition, the combination of ultrasound-controllable mechano-genetics with genetic regulation tools, e.g. CRISPR and Cas9, can allow dynamic genome editing *in vivo* at any location deep in living organisms (6). Integrated with epigenetic modulators and nuclease-deficient Cas9 (dCas9) targeting specific genome locus, this ultrasound-controllable mechano-genetics can be applied to remotely and non-invasively control the locus-specific epigenetic landscapes and Endogenous gene expression profiles (7). It is expected that each component of this ultrasound-controllable mechanic-genetics, i.e. ultrasound controllers and transducers, genetic/epigenetic transducing modules, and mechanic-sensors, will continue to be evolved for greater precision. The leverage of technological advancements of these

different fields into this ultrasound-controllable mechanic-genetics should in turn drive the development of these individual fields to open up new avenues.

We envision that wearable patches carrying ultrasound transducers will be developed in the near future to be controllable by mobile phones and/or control devices via wireless and Internet connection. In fact, stretchable electronic circuits have been developed to produce wearable patches and ultrasound transducer arrays. As such, this ultrasound-controllable mechano-genetics technology will lead to a paradigm shift in translational medicine and pave the way for future telemedicine approaches, providing programmable health care at a remote distance for individual patients transplanted with ultrasound-controllable cells. In summary, our suite of engineered molecular tools laid some groundworks to advance biomedical and clinical applications.

5.2 References

1. Yoon S, Wang P, Peng Q, Wang Y, & Shung KK (2017) Acoustic-transfection for genomic manipulation of single-cells using high frequency ultrasound. *Sci Rep* 7(1):5275.

2. Shaner NC, Steinbach PA, & Tsien RY (2005) A guide to choosing fluorescent proteins. *Nat Methods* 2(12):905-909.

3. Tsien RY (1998) The green fluorescent protein. *Annu Rev Biochem* 67:509-544.

4. Zhang J, Campbell RE, Ting AY, & Tsien RY (2002) Creating new fluorescent probes for cell biology. *Nat Rev Mol Cell Biol* 3(12):906-918.

5. Wang Y, Shyy JY, & Chien S (2008) Fluorescence proteins, live-cell imaging, and mechanobiology: seeing is believing. *Annu Rev Biomed Eng* 10:1-38.

6. Deisseroth K (2015) Optogenetics: 10 years of microbial opsins in neuroscience. *Nature neuroscience* 18(9):1213-1225.

7. Konermann S, Brigham MD, Trevino AE, Hsu PD, Heidenreich M, Cong L, Platt RJ, Scott DA, Church GM, & Zhang F (2013) Optical control of mammalian endogenous transcription and epigenetic states. *Nature* 500(7463):472-476.